STATISTICAL METHODS IN
ULTRASONIC TISSUE CHARACTERIZATION

by

LUIS CARLOS MAAS III

S.B., E.E., Massachusetts Institute of Technology (1992)
S.B., C.S., Massachusetts Institute of Technology (1992)

Submitted to the
Department of Electrical Engineering and Computer Science
in partial fulfullment of the requirements
for the degree of

MASTER OF SCIENCE
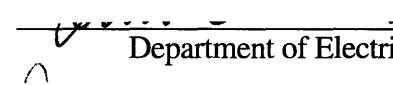
in Electrical Engineering and Computer Science

at the

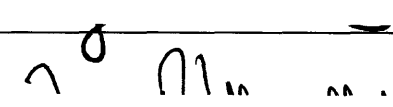## MASSACHUSETTS INSTITUTE OF TECHNOLOGY

May 1994

Signature of Author _____
Department of Electrical Engineering and Computer Science
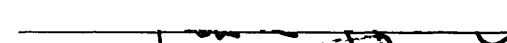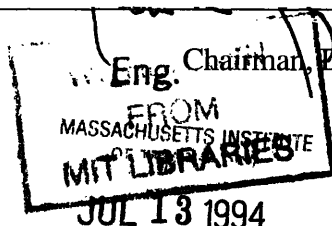May 6, 1994

Certified by _____
Richard T. Lee, M.D.
Thesis Supervisor

Certified by _____
Roger Mark, M.D., Ph.D.
Thesis Supervisor

Accepted by _____
Frederic R. Morgenthaler, Ph.D.
Eng. Chairman, Departmental Committee on Graduate Students

Statistical Methods in Ultrasonic Tissue Characterization

by

Luis Carlos Maas III

Submitted to the Department of Electrical Engineering and Computer Science, May, 1994,
in partial fulfillment of the requirements for the Degree of
Master of Science in Electrical Engineering and Computer Science.

Abstract

An experimental study was carried out to examine the possiblity of using textural information from ultrasonic images to help characterize tissues. Several statistical models of increasing generality for the generation of textural characteristics as quantified by the autocorrelation of the ultrasonic scan information are presented. The final model treats the returning ultrasonic pulse as the summation phasor of a circularly-Gaussian component due to diffuse individual scatterers and a specular component due to structural regularities within the tissue. Several summary statistics of the autocorrelation curve are described. Experimental data from laboratory samples of normal and diseased myocardium collected with commercially available ultrasonic equipment were analyzed. The area under the autocorrelation curve of the normalized image intensities, an image variability-weighted measure of the speckle cell size, demonstrated a significant dependence on the tissue disease group ($p<0.005$ by analysis of variance), indicating that it may serve as a possible characterizing measure. Issues related to real-time data collection from living subjects were also explored. Analysis of the dB-luminance probability distribution from the left ventricular blood cavities of subjects undergoing transesophageal ultrasonic examination revealed an observed mean square error of approximately 5% of mean expected energy, suggesting the feasibility of real-time data collection from living subjects.

Acknowledgements

Table of Contents

4

1. Introduction

Ultrasound is most often used in clinical cardiology in one of two ways. First, analysis of specular echoes arising from the smooth surfaces of the heart allows clinicians to visualize and evaluate the size, shape, and function of the cardiac chambers and valves. Second, quantification of Doppler frequency shift data recorded from red blood cells allows the evaluation of cardiac output and valvular function, and the detection of intracardiac shunts.

In addition to these principal uses, clinicians have long noticed certain textural differences between the appearances of normal and abnormal myocardium in two-dimensional echocardiograms, also known as B-scans. These qualitative observations suggest that clinical abnormalities resulting from variations in the histologic structure of myocardial tissue are associated with variations in measurable acoustic parameters. This evidence is, in turn, a strong motivation for research in ultrasonic tissue characterization, which attempts to classify tissues as normal or abnormal and to indicate the nature of the abnormality based upon ultrasound signals returning from the myocardium.

Because of the simplicity, relative safety, nonionizing and noninvasive nature, low cost, and portability of diagnostic ultrasonic equipment, a system to directly characterize

abnormalities in myocardial tissue using an ultrasonic texture analysis technique would have great clinical utility, and would be safer than invasive surgical techniques or other methods requiring the use of ionizing radiation.

In this thesis report, statistical models for the generation of texture in ultrasonic images are presented and their limitations for tissue characterization explored. A simple model, based upon diffuse random scattering by tissues on principles related to both laser optics and communications theory, describes image texture solely as a function of the ultrasonic beam characterisitics and the average scattering power of the tissue. Useful in characterizing such random materials as unclotted blood, it provides a first step towards a more general model allowing greater flexibility in dealing with structures with a constant underlying order. This intermediate model will then allow the introduction of another general model, known as the Generalized Rician model, also based in part on work in communications theory, which allows the structural component to be described by its statistical properties. Since these models all attempt to predict the autocorrelation function in the direction of the interrogating beam, single-valued summary statistics of the autocorrelation curve are introduced for use in comparing the autocorrelation functions of different tissues.

The principal experimental research in this thesis was designed to test the hypotheses that laboratory samples of the same tissue type, heart muscle tissue, which have been subject to different pathologic processes, will exhibit differences in the characterizing statistics compiled from the autocorrelation curve, and that unavoidable variations in experimental setup can be accurately controlled for. The observed differences in the characterizing statistics are then related back to possible variations in the independent variables of the general statistical model.

Lastly, extension of the experimental design to real-time data acquisition from living subjects is considered. Specific issues introduced by this design are described, and

experimental data is presented to support the feasibility of valid data collection under these

conditions.

2. Ultrasonic Image Generation

2.1 Basic Principles

When an ultrasonic pressure wave propagates through a tissue from a source, sound energy propagates back towards the source whenever acoustic impedance mismatches are encountered. Such impedance mismatches may occur at the interface between two different tissues, or as part of an inhomogeneity within a tissue. The priniciples of reflections and scattering are analogous to electromagnetic principles. For example, if the wavelength of the ultrasound is much smaller than the dimensions of the boundary, such as at the relatively smooth interface between endocardium and blood, a specular reflection occurs. Such reflections are useful for the visualization of the smooth surfaces of the heart. If the mismatch dimensions are much smaller than the wavelength, as in a single blood cell or fiber of collagen, Rayleigh scattering occurs. These scattered waves radiate multidirectionally, and some portion of the resulting wave is directed back towards the transducer, *i.e.* backscattered. In most soft tissues, scattered waves contain much less energy than the incident wave, and hence one can make the simplifying assumption that all wave energy at a point is due entirely to the incident wave and that

10

scattered waves are neglible. [Reid, 1986] This assumption is known as the Born approximation.

2.2 Pulse - Echo Techniques

Overview

Most clinical imaging is performed using pulse-echo techniques, where tissue is insonified with a narrow, pulsed radio frequency (RF) ultrasonic pressure wave from a transducer, typically at 1-10 MHz for diagnostic ultrasound. The returning RF signal is received by the same transducer, converted to an electrical signal, amplified, and processed. An image is constructed by mapping image intensities to the envelope amplitude of the returning wave. Assuming a constant sound speed of 1500-1540 m/s in soft tissue, true distances can be estimated by mapping depth to the "time-of-flight" of the returning wave. By performing a planar sector sweep over a region of interest, a complete image can be constructed, which can be interpreted as a form of reflectivity map for the tissue. The basic process is depicted in Figure 2.1.
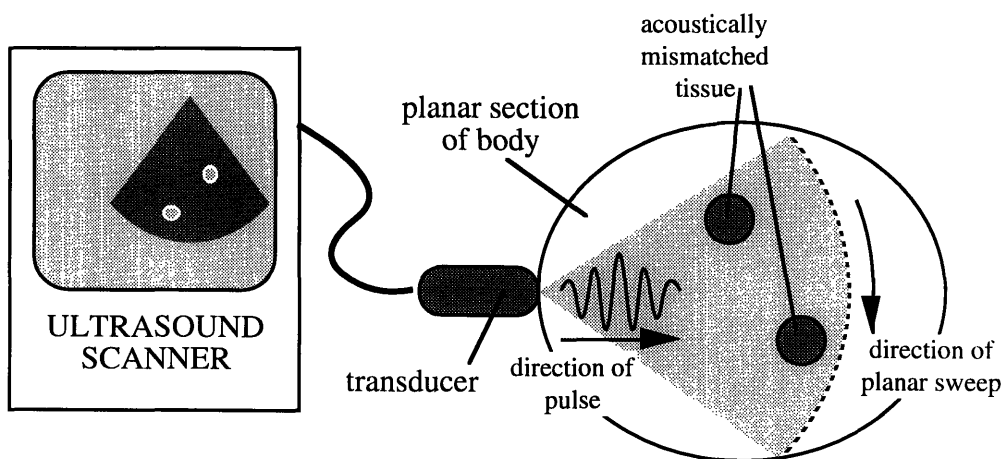
Figure 2.1: Graphical depiction of pulse-echo imaging. Tissue is insonified with narrow wave pulses. The returning RF signal after each pulse is individually processed. After a sector sweep, a 2-D image is constructed. Output image intensity is mapped to the signal amplitude returning from that position. The lightly shaded region within the body wall is insonified by the sweep, and maps to the darkly shaded region of the scanner output.

11

An ultrasonic wave is attenuated as it propagates through soft tissue. Because of internal friction and viscous forces between molecules of soft tissues, absorption is largely caused by a relaxation phenomenon that converts the wave energy into heat. Additionally, scattering by small inhomogeneities in the tissue may contribute to attenuation. In the diagnostic ultrasonic frequency range used in medical imaging, 1-10 MHz, absorption dominates, and scattering is only a small fraction of overall attenuation. However, as in electromagnetic wave theory, ultrasonic scattering is proportional to the fourth power of the frequency used, and thus attenuation increases with increasing frequency. Whereas higher frequencies can provide better image resolution, the price is decreased penetration depth. Attenuation properties of tissues at a given frequency are usually described in terms of the exponential attenuation coefficient α, which is analogous to the loss coefficient for an electromagnetic lossy medium.

Time-gain compensation (TGC) amplification attempts to correct for the attenuation of the signal by tissues. Increasing gains are applied to the signal as it returns from increasing depths. Common clinical equipment allows the operator to adjust the TGC gains for various depth levels individually to obtain the optimal, *i.e.* most visually pleasing, image. On most equipment, the operator also has control over the transmitted power level.

Figure 2.2 depicts the processing of a portion of the received signal following a single pulse from a simulated transducer into a tissue. The received RF signal, also known as an A-Line, is TGC-corrected, then passed through an envelope detector which extracts the echo amplitude envelope.
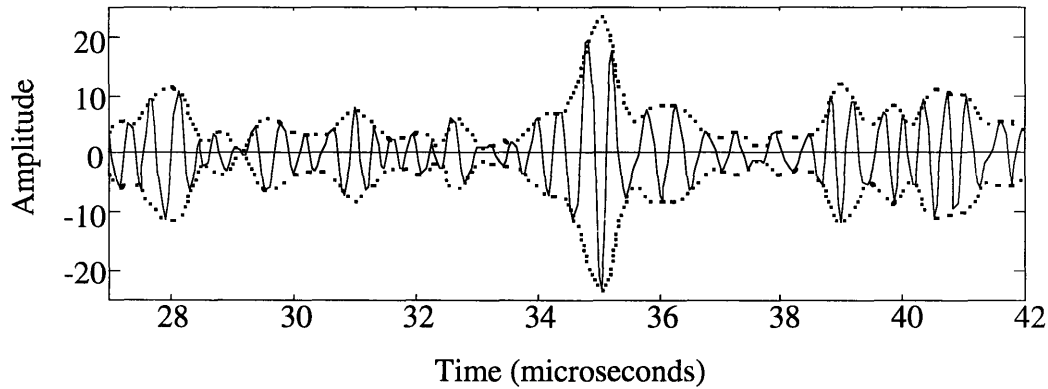
Figure 2.2. Construction of an A-Line. A simulated returning RF wave from a 2.5 MHz transducer has been TGC-corrected (solid wave) and its envelope (dotted wave) is converted to an electric signal. Time axis represents elapsed time since pulse was emitted. Distance from transducer can be determined by multiplying time axis by the speed of sound in soft tissue (1500 m/s) and dividing by 2, since the wave must travel back and forth from the transducer to the region of interest. The entire plot represents approximately 1 cm of signal.

Construction of a two-dimensional image

To create a two-dimensional B-scan, A-line data are collected along many scan lines, typically in a sector sweep. For example, the Hewlett-Packard Sonos 1500 series ultrasound machine used in the experiments reported in this thesis computes 121 A-lines per image in its standard configuration.

To perform the sector sweep, the transducer may be mechanically rotated. However, most common clinical machines utilize an electronic steering mechanism. A real-time phased array transducer system, such as the HP Sonos 1500, directs its beam by appropriately delaying signals from the individual piezoelectric crystal elements of the array, which typically number 64 or 128, to establish a dominant wavefront in a chosen direction. The different lines of the sector scan are produced by altering the direction of the beam formation through an arc. Since image quality at a given depth is also a function of the focus distance of the beam, phased array transducers offer the additional advantage of variable focusing of the beam. Figure 2.3 shows the generation of a narrow pulse in a region of interest using a phased array system.

13
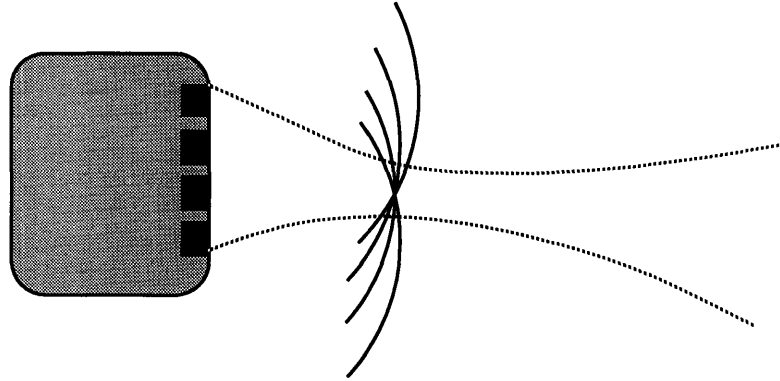
Figure 2.3. The generation of an electronically steered narrow ultrasonic
pulse with a four-element phased array transducer. By varying the delays
introduced into the signal from each element, the beam can be variably
directed and focused during beam generation, or dynamically focused to
receive the returning signal. The two dotted lines represent the effective
width of the beam, which comes to a minimum at the focal distance where
the waves shown all come together and interfere constructively.

A scan converter subsequently transforms data acquired along the various scan lines

into a rectangular (Cartesian) format for output using conventional video displays and

videotape recorders. The HP Sonos 1500 utilizes 64 output gray levels (6-bit resolution).

The scan converter also interpolates missing values to create a continuous image from the

scan lines.

Compression of RF dynamic range

TGC-corrected RF signals from tissues typically occupy about 100 dB of dynamic

range. Since the six-bit equipment used to display the images has about one-fifth the range,

some form of data compression is required [Skorton *et al.*, 1985]. Many machines allow

the operator to choose from various compression schemes. Common settings range from

linear to logarithmic. Since much information is contained in the lower part of the dynamic

range, logarithmic compression is generally preferred so that weak and strong echoes can

be seen on roughly the same scale in the resulting images.

Figure 2-4 shows a simple block diagram for a complete phased array system.
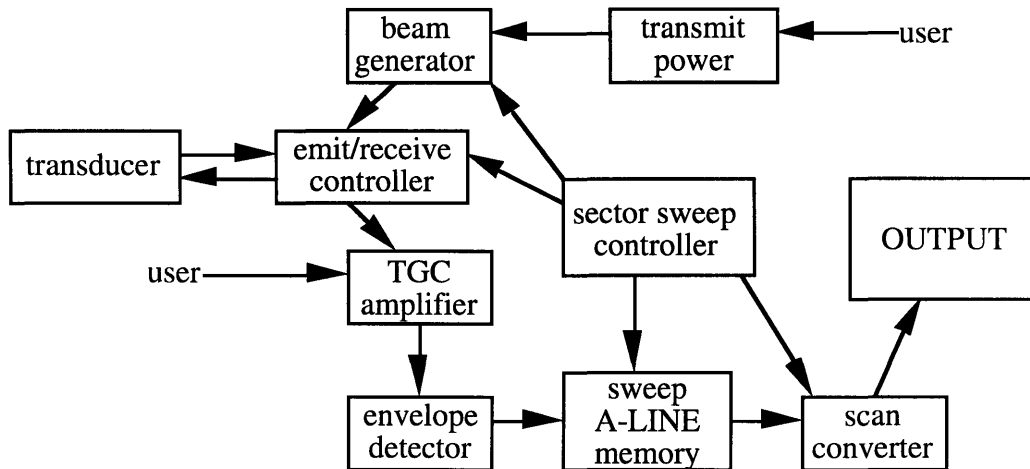
Figure 2.4. Block diagram for a phased array ultrasonic imaging system.

2.3 Relevant physiology

Heart structure and function

The ventricular walls of the heart are made up of many layers of muscle travelling across the ventricles. The layers are composed of cardiac myocytes and fibrous connective tissue rich in capillaries. Since these muscle layers scatter more efficiently than blood in the range of ultrasonic frequencies used in clinical imaging, cardiac tissue appears brighter on average than blood in echocardiograms. Since adjacent muscle layers are oriented at angles up to 90 degrees with respect to one another, the discrete layers of myocardial tissue form relatively smooth surfaces over large areas. As a result, ultrasonic reflections from muscle layers have a specular nature. Not surprisingly, these reflections are dependent on the angle of insonification by the interrogating beam. [Skorton and Collins, 1986]

Collagen is an important constituent of the connective tissue found in myocardial tissue. Collagen is a major structural protein and source of local elastic variation. Since acoustic scattering in tissue is caused largely by spatial variations in elasticity [Fellingham and Sommer, 1984], the distribution of collagen may be an important factor in determining the characteristics of an ultrasonic wave returning from the heart. Although the normal

15

myocardium contains less than 1% collagen per wet weight of tissue, the collagen content of the heart may increase in many disease states, particularly chronic conditions. Increases of over five-fold in collagen concentration have been demonstrated in animal models of chronic infarction and may be linked to the increased backscatter observed in infarcted tissues [Skorton and Collins, 1986].

Acoustic properties of Blood

Blood consists of plasma in which mainly red blood cells, also called erythrocytes, white blood cells, also called leukocytes, and platelets are suspended. Normally 40-45% of the blood volume is filled by cells. This percentage is known as the hematocrit. Red blood cells (RBCs) make up almost all of the cellular volume, numbering approximately 5 million per microliter in a normal adult, more than 700 times more common than similarly sized white blood cells, and 20 times more common than the much smaller platelets. RBCs are shaped like biconcave discs with a mean diameter of 7.5 microns, average maximum thickness of 1.9 microns, and mean volume of 83 cubic mirometers [Guyton, 1991]. Since these dimensions are much smaller than the wavelength of diagnostic ultrasound (approximately 600 microns for a 2.5 MHz pulse in human tissue), the scattering of ultrasonic waves from blood can be predicted to be independent of cell shape and orientation, and isotropic scattering can be expected. Moreover, the position of individual scatterers in blood can be treated as uncorrelated, although it has been suggested that as hematocrit levels increase, contact between scatterers may lead to a more correlated distribution [Shung *et al.*, 1976].

3. Previous Research in Ultrasonic Tissue Characterization

3.0 Background

Research in ultrasonic tissue characterization is usually broken down into two areas: analysis of radio-frequency (RF) data and analysis of B-scan video images.

3.1 RF based approaches

Many methods directly analyze the returning RF data to estimate acoustic parameters which can be used to characterize tissues. The advantages of these approaches are the availability of the raw transducer data with frequency resolution limited only by the sampling equipment. At this early stage, the data are still unaffected by most operator dependent variables such as TGC settings and compression.

One parameter used in RF based tissue characterization is the relationship between attenuation and frequency. It is well known that attenuation of ultrasound by myocardium is due both to absorption and scattering and varies approximately linearly with frequency. Thus, the slope of the attenuation/frequency relationship, typically measured in dB/cm/MHz, has been very well studied. Many investigators have studied the slope of attenuation coefficient versus frequency as a possible characterizing parameter. Lizzi *et al.*

17

[1986, 1992] averaged the power spectra estimated from scan lines in a region of interest and divided by a calibration spectrum derived from the front surface of a flat plate. In theory, this calibrated spectrum technique removes various frequency-dependent transfer functions associated with the electronics of the system and the transducer. Linear regression was used to fit the quasi-linear shapes to estimate the slope of the attenuation parameter. They were able to relate slope to the effective scatterer size, and the average spectral intercept to both scatterer size and acoustic concentration.

Another group of related parameters used to characterize tissues represent various quantifications of backscatttered energy. The backscatter transfer function measures the power spectrum of the returning signal with respect to a standard reflector plate. Integrated backscatter (IB) is the frequency average of the backscatter transfer function, *i.e.* a measure of the total energy in an echo signal. IB measurements have been found to permit the differentiation of normal from ischemic or cardiomyopathic tissues in animal models. [Mimbs *et al.*, 1981] A normally occuring cardiac cycle-dependent variation of IB measurements has also been observed [Madaras *et al*, 1983], and attenuation of this difference in IB between systole and diastole has been related to reduced contractile performance [Wickline *et al.*, 1985], infarction [Vered *et al.*, 1989], hypertensive hypertrophy and hypertrophic cardiomyopathy [Masuyama *et al.*, 1989], and transplant rejection [Masuyama *et al.*, 1990].

Another approach to RF based tissue characterization is direct pattern recognition based on the RF signals. Dyer *et al.* [1986] studied minimum-distance and nearest-neighbor classification schemes based on training set data collected from *in vitro* samples of canine and human hearts. To reduce the dimensionality of their data set, they applied one of four orthogonal transformations, such as the discrete Fourier transform, and kept only those entries with the highest variance between the two sets. Classification accuracy on the order of 75% were achieved.

There are several disadvantages to RF-based methods. First, the returning RF signal must be sampled at a very high rate (10 MHZ or higher), and requires a great deal of storage space for the resulting data. Additionally, processing of such large data sets can be very time consuming. Most importantly, RF-based methods require specialized equipment not normally available in a clinical setting.

3.2 Video based approaches

Other methods directly examine the video images produced by the clinical B-scanner. Such images are readily available in clinical laboratories and can be digitized by easily-accessible video digitizing equipment. Video-based data require much less storage space than the corresponding RF data. Additionally, video images can be stored conveniently on conventional videotape for later off-line analysis.

Video-based methods are based upon qualitative observations made by direct visualization of the images. Clinical echocardiographers have noticed several textural qualities associated with certain physiologic and pathologic states. Examples include increased brightness of echo reflections from scarred tissue in patients with chronic myocardial infarction [Rasmussen *et al.*, 1978], an unusual "ground glass" texture of the myocardium in patients with hypertrophic cardiomyopathy [Martin *et al.*, 1979] (presumably related to the altered myofibrillar architecture of the septum in this disorder) and a peculiar "sparkling" texture in the myocardium in most B-scans of patients with amyloidosis [Siqueira-Filho *et al.*, 1981]. Logan-Sinclair *et al.* [1981] and Parisi *et al.* [1982] have noted increases in displayed echo intensity in regions of fibrosis related to chronic infarction and other injuries, and have used color encoding to facilitate perception of these differences.

Unfortunately, the utility of qualitative descriptions of abnormalities in the appearance of the myocardium on standard B-scans is largely dependent upon the ability of the observer to recognize these abnormalities in gray scale images. Since descriptions of

myocardial texture utilize such subjective qualitative terms as coarse and fine, hypo- and hyper-echoic, or uniform and nonuniform, these approaches are also limited by their subjective nature, the variations in equipment settings, artifacts produced by the imaging system, and the skill of the technician operating the equipment. Compression, TGC settings, reject, damping, imaging depth, transducer frequency, and other operator-determined factors may significantly alter the appearance of image texture, possibly masking "diagnostic" texture distributions or mimicking others [Skorton and Collins, 1986; Thijssen *et al.*, 1990] Additionally, some variablility may be introduced into images during the interpolation required during scan conversion [McPherson *et al.*, 1986].

Nonetheless, since the previously described abnormalities could often be described qualitatively by simple visual inspection of standard images, researchers believe that the information relevant to ultrasonic properties of the tissue may be extracted directly from the images. Hence, there has been much research of objective measures of image characteristics through various quantitative approaches to tissue characterization.

Investigators have attempted to classify the patterns and gray-level distributions of echo images. Skorton *et al.* [1983] analyzed the gray-level histograms of the video images of normal and infarcted myocardium in dogs. The normal myocardium exhibited a peaked, skewed gray-level distribution with high kurtosis value (ratio of the fourth central moment to the square of the variance), whereas infarcted regions exhibited a relatively larger number of higher gray levels, lowering the kurtosis. Other investigators have also studied first-order statistics of images, *e.g.* mean, variance, kurtosis, and skewness [Nicholas *et al.*, 1986]. Hishida *et al.* [1990] found statistically significant differences in the mean, skewness, and kurtosis of normalized gray levels within the interventricular septum of patients with left ventricular hypertrophy, myocardial infarction, and normals. Stempfle *et al.* [1993] have found that acute cardiac rejection in dogs is associated with a progressive increase in the mean gray level of echocardiographic images. Lythall *et al.* [1992] found a completely reversible decrease in the difference between the echo amplitude at end-diastole

and end-systole in the interventricular septum and left ventricular posterior wall during coronary occlusion with an angioplasty balloon. Pingitore *et al.* [1993] found significant reduction of mean gray-level variation in humans developing intraoperative ischemia.

Another area of research is the spatial distribution, or second-order statistics, of the images. Skorton *et al.* [1983] applied gray level run-length statistics, a technique borrowed from satellite terrain classification [Galloway, 1975], and other quantitative texture measures to assess the usefulness of these measures in the diagnosis of the myocardial contusion. They found contused regions characterized by coarser texture as assessed by the quantitative measures of run-length statistics. Chandrasekaren *et al.* [1991] used gray-level run lengths and differences to yield information about the heterogeneity of the image and the relative size of the individual echo reflections and thus characterize the image texture. Using standard videotaped echocardiographic data, they found that quantitative texture analysis can distinguish normal from myopathic myocardium and discriminate between infiltrative and hypertrophic processes. McPherson *et al.* [1986] found significant differences in run-lengths and differences in closed-chest dogs before and after coronary occlusion.

Although much work has been done using some measures of second-order statistical variation, little work has been completed in cardiac ultrasound utilizing the autocorrelation function, a natural measure of texture. Although the texture of an image is highly dependent on the transducer frequency and instrument settings, controlling for these variations should allow for direct comparison between images from different subjects.

4. Speckle Theory

4.0 Background

Much of the work described in the previous chapter reports the observation of various phenomena in data without offering any underlying model for its generation. This work focuses on the autocorrelation function as a quantification of texture characteristics. This chapter introduces models which help to better understand the sources of image texture and to indicate how changes in the underlying tissue structure and composition may lead to changes in the autocorrelation function measured from ultrasonic images.

Texture in ultrasonic images is largely due to interference effects from unresolvable scatterers and is characterized by a granular appearance in ultrasonic images, a phenomenon known as *speckle*. Reflected waves interfere coherently when an ultrasonic pulse encounters many unresolvable scatterers. An early simple mathematical model for ultrasonic speckle was presented by Burckhardt [1978] who extended work in laser optics speckle to ultrasound. Additional insight has been gained through comparison to narrowband noise theories in the field of statistical communications. The random scatterer model first developed by Burckhardt has been carefully studied by many researchers in the field. It treats tissues as a randomly arranged collection of individual scatterers. Wagner *et*

al. [1985] have extended the basic model to include background signals representing underlying tissue structure, using some results from statistical communication theory. This chapter reviews theories from Burckhardt's simple model to Wagner's general model, including some extensions of these theories relevant to clinical ultrasound.

Full derivations of first-order and second-order statistics for these models can be found in Appendix A and Appendix B, respectively. Important steps in the derivations and final expressions for relevant statistics will be presented below. Section 4.1 will present the simple homogenous random media model, where the tissue is treated as a diffuse collection of randomly arranged scatterers. Section 4.2 will cover an intermediate model which permits the addition of a constant background signal to represent an underlying specular structure component of the returning signal. This model will be used as a stepping stone to the general model, presented in Section 4.3, which allows both the diffuse and specular components to be described in terms of their statistical properties.

4.1 Speckle in the Case of Randomly Arranged Diffuse Scatterers

The first model presented considers scattering by a homogenous random medium. The component of the returning signal determined by random scatters is referred to as the *diffuse* component. This model consists of only a diffuse component.

The resolution cell of an ultrasound scanner is defined as the smallest resolvable volume of interrogated tissue. It is the volume bounded axially by the beam pulse length and laterally by the diffraction width of the beam and beam focusing effects. Usually, the cell dimensions are defined by the -6 dB points from the maximum in the directions involved. When more than one scatterer lies in a single resolution cell, the pressure waves returning from the individual sites will interfere coherently when received at the transducer, *i.e.* superposition holds. Such scatterers are said to be unresolvable. This model treats tissues as a collection of randomly distributed unresolvable scatters.

23

Mathematically, the wavelet returning from any one scatterer within a resolution cell can be modeled by a phasor, and the total pressure wave returning from that resolution cell to the transducer face can be represented as the summation of the individual scatterer phasors within the cell. If the phase angle of each phasor is independently and uniformly distributed over the primary interval, as in a random distribution, and the amplitude of each phasor is independent of its phase, then the solution of the sum of the phasors is analogous to the random walk problem in a complex plane [Jacobs and Thijssen, 1991]. For a sufficiently large number of scatterers, one can invoke the central limit theorem, and the distribution for the resultant phasor is a zero-mean circular Gaussian probability density function [Goodman, 1985]. The conditions where these assumptions hold are said to result in "fully developed" speckle. Ohya *et al.* [1992] define the speckle region to exist when more than about 10 scatterers exist within a resolution cell.

For the narrowband pulses used in ultrasound, envelope detection of the returning signal can be modeled by detection of the instantaneous phasor amplitude [Middleton, 1987]. Thus, applying a change of random variables relating the magnitude and phase of the resultant phasor to its complex components, the marginal probability density functions (PDFs) for the envelope amplitude E and intensity I of the theoretical distribution, as modeled by the amplitude and squared-amplitude of the summation phasor, can be easily solved. These simple PDFs are known as the Rayleigh and negative exponential PDFs, respectively, and are presented in Equations 4.1 and 4.2 for envelope amplitude E and intensity I, where the parameter ψ is a measure of the mean-square scattering strength of the tissue, equal to the variance of the real and imaginary Gaussian phasor components [Goodman, 1975].

$$p_E(E) = \frac{E}{\psi} \exp\left\{-E^2/2\psi\right\}, \qquad \text{for } E \geq 0. \qquad [4.1]$$

$$p_I(I) = \frac{1}{2\psi} \exp\left(-I/2\psi\right), \qquad \text{for } I \geq 0. \qquad [4.2]$$

From these PDFs, the following important quantities can be solved [Papoulis, 1991]:

$$\langle E \rangle = \sqrt{\frac{\pi \psi}{2}}$$

$$\langle E^2 \rangle = \langle I \rangle = 2\psi$$

$$\langle E^4 \rangle = \langle I^2 \rangle = 8\psi^2$$

$$\sigma_E^{\ 2} = \frac{(4 - \pi)\psi}{2}$$

$$\sigma_I^{\ 2} = 4\psi^2 = \langle I \rangle^2 \qquad\qquad [4.3\text{-}7]$$

An important characteristic of these PDFs is their constant signal to noise ratio (SNR). By calculating the ratio of the expected standard deviation to the expected value as a function of ψ, the envelope SNR is determined to be approximately 1.91, and the intensity SNR is unity, both independent of ψ. Experimental studies [Smith *et al.*, 1982; Foster *et al.*, 1983] have found measured SNRs in computer simulations or tissue mimicking phantoms in agreement with these theoretical values. Thus, a constant SNR can be used as a test of agreement with the underlying model. Additional implications of a constant SNR will be discussed later.

The Log Compressed Rayleigh Distribution

To date, there is a lack of significant amount of research or experimental data clearly demonstrating the possibility of extracting scatterer characteristics from the compressed signals normally encountered in commercially available B-scanners [Waag *et al.*, 1991]. The statistics for such a system, however, can be derived from the above solutions. Since these statistics will be used later to assess some of the issues of real-time data collection from real subjects, they will be developed here. For the case of fully logarithmic compression, the following substitution is made:

$$B = C \log_{10} E = C \log_{10} \sqrt{I}. \qquad\qquad [4.8]$$

If the result is expressed in decibels, $C=20$. The following PDF for compressed image strength as a function of scattering strength ψ and coefficient C is obtained through statistical transformation of Equation 4.1 or 4.2:

$$p_B(B) = \frac{\ln 10}{C\psi} \exp\left\{ \frac{2B\ln 10}{C} - \frac{\exp(2B\ln 10/C)}{2\psi} \right\} \qquad \text{for } -\infty < B < +\infty. \quad [4.9]$$

This PDF, which will be referred to as the log compressed Rayleigh distribution, is characterized by identically shaped curves with means increasing for larger values of ψ. Some of these curves are presented in Figure 4-1. The power-level independent shape of the resulting family of PDFs is a manifestation of the ψ independence of the expected standard deviation of the transformed PDF. This reflects the fact that the logarithmic transformation converts the signal dependent noise of the original estimates into additive noise. Thus there is constant variance within this family PDFs [Steinmetz *et al.*, 1992]. A similar statement was made by Burckhardt [1978] who noted that the fixed signal to noise ratio of magnitude required the noise to be converted to additive noise upon logarithmic compression. In Appendix A, the variance is verified to be independent of ψ and approximately equal to 31 square-decibels.
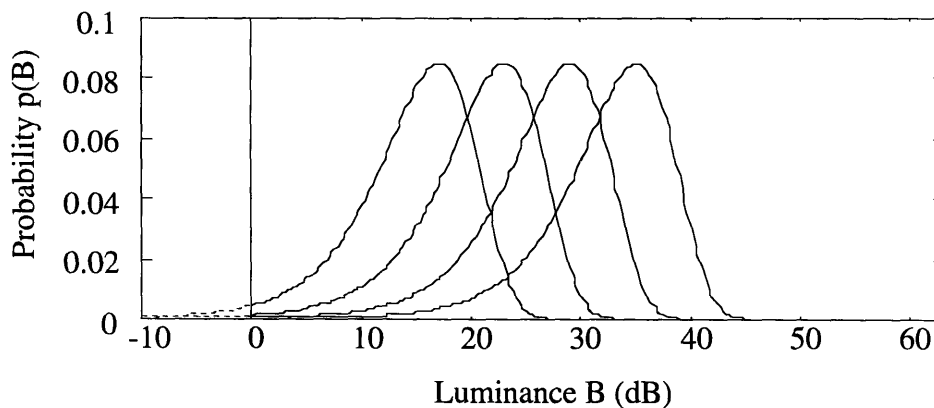
Figure 4-1: Log compressed Rayleigh distributions from Equation 4.4 for different values of ψ with $C=20$, *i.e.* compression to decibels. From left to right: $\psi=25$, $\psi=100$, $\psi=400$, $\psi=1600$ normalized scattering power units. Dotted regions would be clipped to zero on a six-bit system (see text).

It is also possible to calculate the expected theoretical value of B as a function of ψ with $C=20$:

$$\langle B \rangle_\psi \approx 0.5035 + 10\log_{10} \psi. \qquad [4.10]$$

As expected from the description above, the expected value is a simple function of ψ, one which varies linearly with the compressed tissue scattering power in decibels.

On the six-bit system used in this research, only the integer range of values $0 \le B \le 63$ are defined, with values outside of this range clipped to the bounds. This is represented by the dotted segments of the PDFs in Figure 4-1. The expected value of Equation 4.5 is valid over the wide range of ψ where high and low clipping are minimized.

Second-Order Statistics of the Diffuse Model

Second-order statistics are useful to describe the qualities of texture. This research focuses on the autocorrelation function to quantify textural differences. These statistics can be determined in both the axial and lateral directions. The lateral statistics are influenced by diffraction and focusing of the beam, both functions of imaging depth, whereas the axial statistics are influenced primarily by the pulse envelope waveform, which is effectively unchanged with depth. For these reasons, this work will focus only on the axial autocorrelation function. To minimize diffraction and focusing effects, all images of interest will be taken near the focal depth of the transducer, and a constant beam width will be assumed.

Use of these functions to describe the texture of the myocardium and other B-scan regions is based on the assumption that the tissue can be treated as a wide-sense stationary system, that is, that all the statistical parameters relating two points are completely determined by the two-dimensional separation between the two points, and not by their absolute positions. Complete derivations and references of the equations presented in this section can be found in Appendix B.

27

Properties of the System Point Spread Function

The transducer point spread function (PSF) can be modeled as separable into two terms: an axial component and a radial component. While the lateral component is a depth-dependent function of diffraction and focusing effects, the axial component can be modeled as a constant characteristic of the system, specifically the waveform envelope of the pulse. For a transducer with a symmetrical usable bandwidth around its center frequency, created by the proper use of damping materials along the piezoelectric crystal, such waveforms can be approximated by a Gaussian window applied to a continuous wave of the center frequency. Thus the axial PSF can be modeled by a Gaussian PSF of an appropriate width centered at the middle of the pulse. A typical -6 dB pulse width for an imaging transducer is on the order of two wavelengths [Jacobs and Thijssen, 1991]. Shorter envelopes are physically difficult to generate, and longer ones sacrifice resolving power.

Thus, the axial PSF g can be modeled as a purely real function [Wagner, 1983] symmetric about $r = 0$, such that $g(r) = g(-r)$.

Autocorrelation of the Complex Phasor

Let A be the complex amplitude phasor for the returning wavelet described previously. The autocorrelation of this random variable is defined as:

$$R_A(\Delta r) = \langle A(r) \cdot \overline{A}(r + \Delta r) \rangle \qquad [4.11]$$

where the overbar indicates complex conjugation of this complex variable. Rewriting A as the convolution of the scatterer position-strength process R and the point spread function (PSF) g of the system yields:

$$A(r) = R(r) * g(r), \qquad [4.12]$$

where the asterisk denotes the aperiodic convolution operator of linear systems. The PSF g is a nonrandom characteristic of the imaging system, and R will be modeled as a stationary process, such that the autocorrelation function of A can be rewritten as:

$$R_A(\Delta r) = g(-\Delta r) * \overline{g}(\Delta r) * R_R(\Delta r).$$ [4.13]

Furthermore, the function R can be separated into two parts:

$$\begin{aligned} R_R(\Delta r) &= \left\langle R(r) \cdot \overline{R}(r + \Delta r) \right\rangle \\ &\approx R_0^{\ 2} \cdot \mu_R(\Delta r) \end{aligned}$$ [4.14]

where R_0^2 is the average scattering strength of R and μ is the normalized short-range internal autocorrelation. Combining Equations 4.13 and 4.14:

$$R_A(\Delta r) = R_0^{\ 2} \cdot g(-\Delta r) * \overline{g}(\Delta r) * \mu_R(\Delta r).$$ [4.15]

This model assumes that the microstructure is random and uncorrelated, $i.e.$ $\mu_R(\Delta r) = \delta(\Delta r)$, the Dirac delta function, such that the internal autocorrelation can be canceled in the convolution of Equation 4.15. Additionally, since g is real and symmetric about zero, Equation 4.15 can be further simplified to:

$$R_A(\Delta r) = R_0^{\ 2} \left[g(\Delta r) * g(\Delta r) \right]$$ [4.16]

Thus the speckle texture in the diffuse model, as characterized by the autocorrelation of the complex phasor, carries only information about the system PSF and average scattering strength. With respect to ultrasonic tissue characterization, tissues that produce fully developed speckle can be characterized entirely by their average scattering strength. For a Gaussian g, the autocorrelation will also have a Gaussian shape. Note that for $\Delta r = 0$, Equation 4.16 is equivalent to the expected value of the intensity I, which was found in Equation 4.4 to be 2ψ:

$$R_A(0) = \left\langle A\overline{A} \right\rangle = \left\langle I \right\rangle = 2\psi$$ [4.17]

Thus, if g is defined such that the second term of Equation 4.16 is equal to one, *i.e.* the PSF g_0 has unit total power, then the constant term in Equation 4.16 can be related to the mean tissue scattering power ψ, using Equation 4.17, to yield:

$$R_A(\Delta r) = 2\psi\left[g_0(\Delta r) * g_0(\Delta r)\right] \qquad [4.18]$$

Autocorrelation of the Intensity

Since the phasor A cannot be determined from the ultrasonic image, an expression for the autocorrelation for phasor amplitude E or intensity I must be derived. Approaches to this transformation include approaches from statistical communication theory [Middleton, 1987], laser optics [Goodman, 1975], and application of the Gaussian moments theorem. These approaches are outlined in Appendix B. Only the resulting theoretical autocorrelation function for the intensity I, the variable used in the experiments of this research, is presented here:

$$R_I(\Delta r) = I_d^2\left(1 + |\rho(\Delta r)|^2\right). \qquad [4.19]$$

In this equation, $I_d = \langle I \rangle = 2\psi$. The subscript d has been added to indicate contributions from the diffuse component of the tissues. A specular subscript will be introduced in later models. The variable ρ is the normalized phasor autocorrelation, also known as the complex coherence factor. It is defined as:

$$\rho(\Delta r) = \frac{R_A(\Delta r)}{R_A(0)} = \frac{R_0^2 \cdot g(\Delta r) * g(\Delta r)}{\langle I_d \rangle} = g_0(\Delta r) * g_0(\Delta r). \qquad [4.20]$$

4.2 An Intermediate Model: Constant Structural Component

The purely diffuse model of Section 4.1 can be extended to add a component resulting from underlying structure within the tissue. Assuming that in addition to random scatterers, the tissue now has a microstructure on a dimensional order smaller than the

30

pulse length of the beam, *i.e.* it is unresolvable. Such a structural component will give rise to a "distributed specularity" [Wagner *et al.*, 1987]. If the microstructure is regular, *e.g.* a regularly spaced lattice of scatterers, the specular component phasor would be a function of the spacing and orientation of the lattice. For proper orientation and spacing, this structural phasor component has constant length and phase. In this intermediate model, the distributed specular component, *i.e.* structural component, is modeled as a constant at all positions. This can be incorporated into the previous model by adding a fixed phasor of length S to the summation phasor of each resolution cell. Without loss of generality, the angle of the phasor can be fixed at zero.

As before, the returning phasor A has a circularly Gaussian distribution, but in this case the mean is not zero, but is offset by the constant structural phasor. Applying the same transformation of variables as above, the following PDF is obtained for the intensity I:

$$p_I(I) = \frac{1}{2\psi}\exp\left\{\frac{-(I+S^2)}{2\psi}\right\}I_0\left\{\frac{S\sqrt{I}}{\psi}\right\} \quad \text{for } I \geq 0. \qquad [4.21]$$

where $I_0(...)$ is a modified Bessel function of the first kind and zero order, and S is the amplitude of the constant phasor. This distribution is known as the modified Rician PDF, since I is the square of the Rician random variable E. The following moments can be determined from this new distribution:

$$\langle I \rangle = 2\psi + S^2 = I_d + I_s$$
$$\sigma_I^2 = 4\psi^2 + 4\psi S^2 = \sigma_{I_d}^2 + 2I_d I_s. \qquad [4.22\text{-}23]$$

In these expressions, the constant I_s has been introduced to represent the contribution to intensity from the structural component, where $I_s = S^2$. The SNR for this model is no longer unity. Instead:

$$SNR = \sqrt{\frac{I_d^2 + 2I_d I_s + I_s^2}{I_d^2 + 2I_d I_s}}. \qquad [4.24]$$

Note that there is a corresponding increase in the SNR relative to the purely random condition, such that it must be greater than unity for nonzero structural components. In an experimental study by Tuthill *et al.* [1988], the SNR was shown to have maxima for microstructural spacing at integer multiples of the transducer base wavelength where constructive interference is maximized, up to the pulse length used (four wavelengths), and minima at non-integral half-multiples where destructive interference dominates. Above the pulse length, SNR decreased as resolvability increased, *i.e.* there was no distributed specularity, only resolvable specularity with increasing amounts of purely "diffuse space" in between.

4.3 The Generalized Rician Model: Stochastic Structural Contribution

The intermediate model of Section 4.2 assumed a constant background distributed specularity added to the returning signal, consistent with very regular microstructure spacing. Real tissues, however have a much less regular structural spacing, and may contain both resolvable and unresolvable parts. The final model, in which the structural component is modeled statistically, has been called the Generalized Rician Model by Wagner *et al.* [1988]. In this model, the diffuse scattering component continues to be described in terms of the diffuse tissue mean-square scattering power ψ, but now the additive distributed specular component is described in terms of its statistical properties, *i.e.* the tissue is now defined by the statistical properties of both its diffuse and distributed specular components. Important first-order statistics are derived in Appendix A. The mean and variance are:

$$\langle I \rangle = 2\psi + \langle I_s \rangle = I_d + \langle I_s \rangle$$
$$\sigma_I^2 = 4\psi^2 + \sigma_{I_s}^2 + 4\psi\langle I_s \rangle = \sigma_{I_d}^2 + \sigma_{I_s}^2 + 2I_d\langle I_s \rangle. \qquad [4.25\text{-}26]$$

In this model, I_s is no longer a constant, but rather defined by its statistics. Note that the expected value of intensity I has the same form as in the intermediate model, but the

32

intensity variance has a new term incorporating the variance of the specular component into the system. The SNR in this model now depends on the SNR of the specular component. Specifically, for specular SNR less than unity, the total intensity SNR will also be less than unity, and vice-versa. Clearly, the degree of change will also depend on the relative magnitudes of the specular and diffuse contributions as compared to signal and variance.

The autocorrelation function for intensity I is found in appendix B:

$$\langle I_1 I_2 \rangle = I_d^2 \left[1 + |\rho|^2 \right] + 2I_d \langle I_s \rangle + \langle I_{s1} I_{s2} \rangle + 2I_d \langle r_1 r_2 + i_1 i_2 \rangle \rho. \qquad [4.27]$$

The variables r and i are the statistically defined real and imaginary parts of the specular phasor component. The autocovariance can be found by subtracting the square of the mean in Equation 4.25 from Equation 4.27. The result is:

$$C_I = I_d^2 \rho^2 + \langle I_{s1} I_{s2} \rangle - \langle I_s \rangle^2 + 2I_d \rho \langle r_1 r_2 + i_1 i_2 \rangle. \qquad [4.28]$$

5. Experimental Methods

5.0 Experimental Outline

Three sets of experiments were performed. A first set of preliminary experiments was performed to assess the noise effects of the videotape storage medium on the data. A second set of principal experiments was designed to examine the dependence of certain summary statistics of the autocorrelation on the pathologic classification of a number of human cardiac autopsy specimens under very controlled conditions. Finally, a last set of experiments was performed to study some of the issues involved in real-time data collection in patients.

5.1 Equipment

The experimental setup used in each set of experiments was identical. A Hewlett-Packard (HP) Sonos 1500 ultrasonic scanner was used to collect standard B-Mode images with a standard transducer for subsequent analysis. Several transducers were used, specifically: an HP model 21364A 5.0 MHz 64-element transesophageal multi-plane phased-array transducer, and both 5.0 MHz and 2.5 MHz 128-element transthoracic phased-array transducers. These pieces of equipment are commonly available clinical tools.

For storage on videotape, the video output of the scanner was connected directly to a Panasonic AG-7350 Super-VHS video cassette recorder with 75 Ohm coaxial cable. The images were recorded onto Super-VHS video cassettes at the fastest standard VHS recording speed. A different VCR of the same model was used for playback. Output was also via 75 Ohm coaxial cable.

Images were digitized using a PCVISION*plus* model PFGPLUS-640-3-60 frame grabber from Imaging Technology, Inc. which captured 640x480 pixels per frame. The digitizing board was installed in an Intel-486 based PC system. The image acquisition software used was the OPTIMAS video package from BioScan, which had been calibrated against the direct output of the scanner, by analyzing known video standards produced by the scanner. Images from the frame grabber were viewed on a Sony PVM-2030 Trinitron color video monitor using RGB inputs from the frame grabber.

Digitized image data was stored on the PC hard disk drive in the standard tagged image file format (TIFF). Signal processing was performed using MATLAB 4.0 by The MathWorks, running on the same PC. Statistical analysis was performed using STATA by Computing Resource Center, also on this PC.

Ultrasound Scanner Calibration

Before recording any data, the scanner settings were set to the standardized values listed in Table 5-1.

Table 5-1: Standard Scanner Settings

Parameter	Setting
Preprocessing	2 (linear)
Persistence	0
Compression	logarithmic
Postprocessing	A (linear)
Transmission Power	variable†
TGC	variable†

†The adjustment of these variable settings is described in the text.

The transmission power dial and time-gain compensation (TGC) sliders were adjusted to obtain the most visually pleasing picture, *i.e.* one of relatively uniform contrast and brightness at all depths, without any obvious low- or high-clipping of data. The significance of these settings and operator-dependent variabilities is described in Chapter 7.

5.2 Videotape Noise Experiments

Data Collection

A normal male subject was imaged in the transthoracic parasternal long axis view using the 2.5 MHz transthoracic transducer. If power levels were adjusted to image heart tissue, as in normal imaging, the blood, a much less efficient scatterer than the tissue, would return signals in the lowest part of the dynamic range, below the levels displayed on the output, and would hence be clipped to zero. To properly image the texture of the blood cavity, the gray-level within the blood cavitity was increased to make the texture visible by increasing the transmitted power and the TGC gains. (Of course, in this setting, the heart tissue will now typically exceed the dynamic range of the output, and be clipped to the output's highest value.) Using the loop-capture function of the ultrasonic equipment, one

half of a second (15 frames) of real-time data was collected and stored by the ultrasound machine. These frames were individually digitized, bypassing the videotape apparatus, and stored as the *reference* frames. Then, each frame was recorded onto videotape for several seconds, and the VCR playback images were digitized and stored as the *video* frames. The images were checked visually to insure proper vertical registration, *i.e.* that each row of data in each video frame matched the corresponding row in the reference frame.

Identical 16x16 pixel regions were selected from each pair of frames. The regions were chosen to lie entirely within the blood cavity. A new signal, the *video error* signal *e*, was defined as:

$$e[n_1,n_2] = v[n_1,n_2] - r[n_1,n_2] \qquad [5.1]$$

for all positions $[n_1,n_2]$ in the 16x16 pixel samples, where *v* and *r* were the video and reference frames, respectively. The error *e* was computed for each of the 15 pairs of frames.

Data Analysis

A probability distribution estimate of the error signal *e* was computed from the 3840 sample values obtained (15 frames of 256 pixels each) for visual inspection, along with the overall mean error and its standard deviation. Using a model where error signal was stationary with respect to position, but *not* with respect to reference signal strength, the expected value μ and standard deviation σ of the video error *e* as functions of the reference signal strength *r* were estimated using linear regression models. The standard deviation model was calculated using standard deviation estimates at each reference signal strength value where 5 or more samples were available, with each such estimate equally weighted. This standard deviation model was then used to calculate the expected signal to noise ratio as a function of reference signal strength.

Assuming constant variance, a corrected error signal with stationary mean was defined as:

$$e_0[n_1,n_2] = e[n_1,n_2] - \hat{\mu}_e\big(r[n_1,n_2]\big) \qquad [5.2]$$

where $\hat{\mu}_e(...)$ is the estimate of the error mean as a function of reference signal strength as determined by the model computed earlier. The vertical autcorrelation of $e_0[n_1,n_2]$ and the crosscorrelation of $e_0[n_1,n_2]$ with $r[n_1,n_2]$ were then estimated.

5.3 Pathology Lab Study

Data Collection

Specimens included sections of histologically classified hearts fixed in a 10% formalin solution. The specimens were individually placed into a 0.9% saline water bath measuring approximately 50x30x12 cm at 37 degrees Celsius. Data were collected using the 5.0 MHz transthoracic transducer placed inside a latex sheath to protect it from water damage. Both the transducer and the sheath were previously treated with acoustic coupling gel. The covered transducer was aimed down the long axis of the bath approximately 4 cm below the surface to minimize reflective noise from the bath borders. The specimens were positioned approximately 2 cm from the transducer atop a plastic support structure resting on the bottom of the water bath. The samples were positioned by hand during the data acquisitions, and all obvious air bubbles were eliminated.

Specimens were examined in two experimental sessions. Seven specimens were imaged in the first session, and fifteen in the second. Descriptions of the hearts used are presented in Table 5-2. The variable settings were adjusted for the first specimen of each session, and were left unchanged for subsequent samples in each session. The zoom mode of the ultrasonic scanner was used for maximum video resolution. For each heart specimen, image views were collected from three different regions of the left ventricular

heart wall. In each view, the heart was oriented such that the surface of the outer wall was as normal to the transducer beam as possible as determined by visual inspection of the sharp water-tissue interface echo. With the heart properly positioned, the scanner's freeze function was employed to hold the image. This frozen output frame was then recorded for several seconds onto the video tape. Data were identified by the sample number of the specimen only, to prevent unintentional biasing.

Table 5-2. Description of Imaged Samples

Group	Session 1	Session 2
Normal	1	2
HCM	1	2
Amyloid	2	3
LVH	0	2
IDCM	2	3
RCM	1	0
Cyclophosphamide	0	1
Myocarditis	0	2
Total	7	15

CM=cardiomyopathy; HCM=hypertrophic CM; LVH=left ventricular hypertrophy; RCM=restrictive CM (non-amyloid), IDCM=idiopathic dilated CM.

Image Processing

Statistical analysis was ultimately performed on corrected final images derived from the digitized sample views. The process of generating these final images, described below, is summarized in Figure 5-1.

select region

estimate
video error

Intermediate Image

subtract

Digitized Image

convert from dB to
intensity units

compute
mean

subtract

correction curve

compute mean &
deviation curve

normalize

lowpass

other session
deviation curves

compute
session average

Final Corrected Image
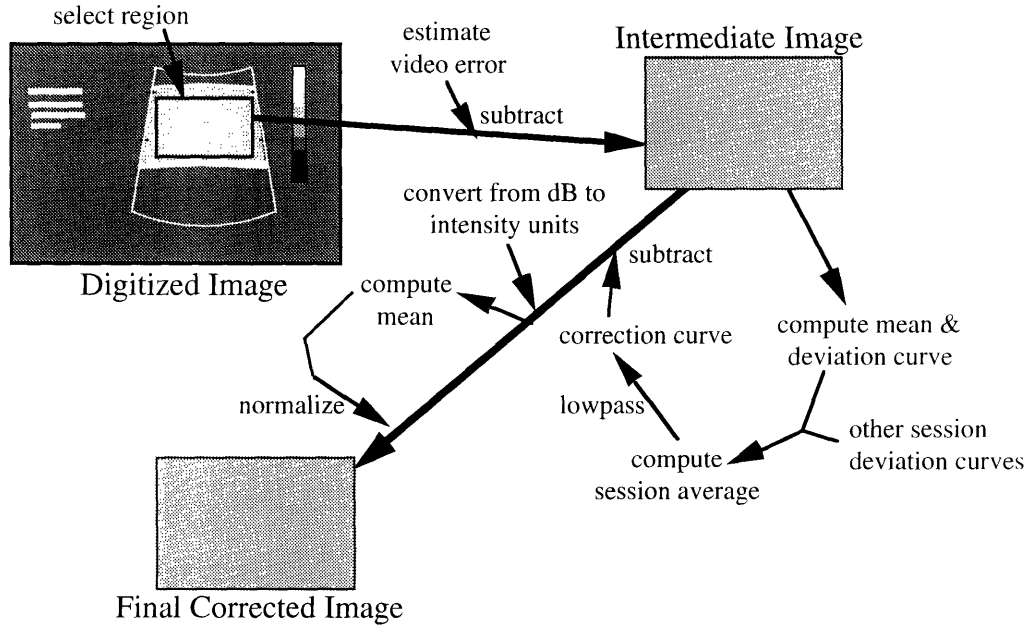
Figure 5-1: Summary of the generation process for the final corrected
images used in the statistical analysis. The steps are described in the text.

New images were generated by selecting regions of interest from each digitized
sample view which included as much of the myocardium as possible in a rectangular
region, while excluding the sharp water-tissue boundary echos. If no suitable region was
attainable, the view was not included in subsequent analysis. These images were corrected
to account for the expected video noise error as determined in the first set of experiments.
Specifically, each pixel value was corrected by the expected error computed by inverting
the linear video error model from above to reflect expected error as a function of measured
video signal strength.

For TGC normalization, a session correction curve as a function of depth, *i.e.*
vertical position, was subtracted from each image collected during that session. This
correction curve was determined by lowpass filtering the average of the deviation curves
for each intermediate image in a given session. Before filtering, the average was corrected
to account for the varying number of samples at each depth resulting from the variable
sizing of the intermediate images. For each image, the deviation curve represents the
average deviation at each depth, *i.e.* vertical position, of the received signal from the total

image mean. The lowpass filter was an 11-point moving average filter. The first and last 5 points of the average were retained unchanged, and the middle kernal was replaced by the moving average output.

At this point, the corrected video signal v' was transformed from the scaled decibel units attained using the scanner's logarithmic compression to the intensity units used in the derivations in Chapter 4. The corrected data were first converted to true decibels by dividing by four, since the frame grabber generates 6-bit data in the highest bits of its 8-bit output, setting the lowest bits to zero, *i.e.* the data is output as integer multiples of four. These decibel values were then directly converted by dividing by 10 and computing the inverse logarithm to base 10. This transformation is given by Equation 5.3:

$$I = 10^{(v'/4)/10} \qquad\qquad [5.3]$$

To convert to normalized values, the resulting images were then divided by the resulting mean intensity value. These final unitless normalized values constituted the final corrected images on which subsequent analysis was performed.

Data Analysis

For each session, the resolution, in pixels per centimeter, was computed by measuring, in pixels, the separation between the scanner calibration markings in the original digitized images. The calibration markings are included at 1 cm intervals. The resolution was computed using the outermost calibration markings for accuracy.

An unbiased estimate of the vertical autocorrelation function for each corrected image was computed. For ease of coding, a biased estimate was first extracted from the biased two-dimensional autocorrelation as computed by two-dimensional Fourier techniques. This estimate was then scaled to remove bias. Since the mean value of the image was set to unity during normalization, the autocovariance is simply one less than the

autocorrelation at each lag, *i.e.* the autocovariance is the autocorrelation minus the square of the mean.

Four summary statistics were computed from the autocovariance estimate. Two of these statistics are depicted graphically in Figure 5-2. All lag distances were converted to millimeters using the computed session resolutions. The maximum value, abbreviated *max*, was defined as the autocorrelation value at zero lag, *i.e.* the mean square intensity. The full-width at half-maximum, abbreviated *fwhm*, was found by linear interpolation between data points as twice the distance between the zero-lag point and the minimum positive lag at which the autocovariance was half of the maximum value. The area under the curve, abbreviated *auc*, was found by taking the sum of all autocovariance values at lags between zero and 5 millimeters equivalent distance, scaled by the appropriate interval length. This sum is an estimate of the integral of the autocovariance from 0 to 5 millimeters. The area to maximum ratio, abbreviated by *a/m*, was found by dividing the area under the curve *auc* by the maximum value *max*.
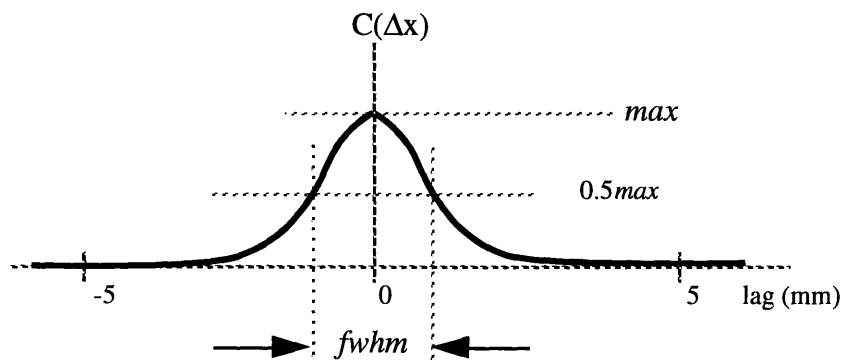
Figure 5-2: Graphical depiction of the summary statistics derived from the autocovariance curves. The abbreviations used are described in the text. The area under the curve is simply the area under the autocovariance between -5 and 5 mm lags.

To assess the dependence of the autocorrelation on pathologic group, multiple linear regression models were generated for each of the summary statistics found above. Restrictive cardiomyopathic and idiopathic dilated cardiomyopathic samples were not included in the test set. The test set contained the normals, and the diffuse processes left

42

ventricular hypertrophy (LVH), hypertrophic cardiomyopathy (HCM), amyloidosis, myocarditis and cyclophosphamide damage. A separate model was generated for each session, where the pathologic grouping and the heart specimen were the independent categorical variables, with the heart specimen nested within the group. The summary statistic of interest served as the dependent variable. Additionally, another model controlling for session was generated by adding the session as another independent categorical variable. Thus, three models were computed for each of four summary statistics.

The significance of the regression models and the significance of the group variable within each model were found by standard analysis of variance. Significance was noted for p values less than 0.05, *i.e.* 95% confidence.

5.4 Transesophageal Echocardiography (TEE) Study

Data Collection

For transesophageal examinations, subjects were patients of the Brigham and Women's Hospital (BWH) undergoing thoracic surgery. The data were prospectively collected in the operating room with a 5.0 MHz transesophageal multi-plane phased-array transducer. Data were collected preoperatively in standard B-Mode form and stored on the videotape in real time. On pause-mode playback, data were collected from every other frozen video frame, i.e. 1/30th second increments, using the frame-by-frame search of the VCR.

A set of image data was recorded from each subject onto video-tape for subsequent analysis. The same machine standardizations were used as in the Pathology Lab experiments. TGC and gain settings were adjusted for each view of each patient to optimize the images.

All data were recorded from the transgastric view with the multi-plane transducer set at zero degrees. A zoom mode segment was recorded at the maximum zoom for the blood cavity. The gains and transmission power were adjusted as in the first experiments so that the speckle patterns in the blood cavity were visible. In each subject, at least three cardiac cycles were recorded.

Image Processing

At least 25 consecutive frames of 128x128 pixel data were digitized for the zoom mode images of the blood cavity, attempting to exclude as much as possible of the myocardium in the data. The images were collected in TIFF format and stored on hard disk for later analysis.

The regions of interest were collected as close as possible to the center of the scan region, such that the vertical direction would closely approximate the true axial direction of the scan lines used to create the B-mode image.

Data Analysis

For the blood cavity data sets, histograms were computed for 10x10 subregions in the center of the blood cavity over the entire data set. The histograms were normalized such that the area included in the histogram summed to unity for direct comparison with the theoretical log-compressed Rayleigh distribution. The theoretical model curve was fit to the data in two ways. First, the theoretical scatterer power parameter ψ was computed from the observed histogram mean using the equation for expected value as a function of the logarithm of ψ as found in Chapter 4. Second, the total-square error was minimized with respect to scatterer power ψ. The total square-error (*TSE*) was employed as a measure of accuracy for the model and was defined as:

$$TSE = \sum_{n=0}^{63} \left\{ hist[n] - p_B(B=n) \right\}^2 \qquad\qquad [5.3]$$

where *hist*[*n*] is the histogram function for the discrete bins $n=0..63$ and $p_B(B)$ is the theoretical probability density function at the discrete value $B=n$, i.e. the value of the PDF at $B=n$ was used as an approximation to an equivalent probability mass function (PMF) at each point. The *TSE* was expressed as a percentage of the total energy (*TE*) in the distribution, approximated by:

$$TE = \sum_{n=0}^{63} \left\{ p_B(B) \right\}^2 . \qquad\qquad [5.4]$$

Thus, the TSE as a percentage of TE is used as a measure of the error. Additionally, values for chi-square goodness-of-fit tests were found for the observed data.

6. Experimental Results

6.1 Videotape Noise Experiments

First order statistics

The video error e was defined as the difference between an image recorded to video and digitized on playback and the same image digitized directly from the ultrasound scanner. The mean and standard deviation of the video error function e were computed from the fifteen frames of video and direct-line data. Mean was $\mu=0.4044$ decibels, and standard deviation was $\sigma=2.48$ decibels. The normalized histogram of the error function is presented in Figure 6-1 along with a Gaussian distribution having mean and standard deviation matched to the experimental values μ and σ. The noise appeared to have some Gaussian-like characteristics.
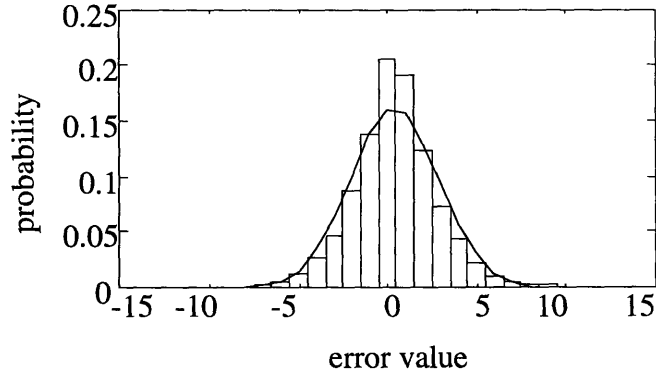
Figure 6-1: Raw videotape error signal. The bar plot indicates a normalized histogram of error values computed from 3840 samples collected over 15 different images. The solid line represents a Gaussian distribution with mean 0.4044 dB and standard deviation 2.48 dB.

A negative covariance between the signal and the error at a given position was found. The mean error e as a function of signal strength s was estimated by linear regression ($p<0.0001$) as:

$$\hat{\mu}(s) = 4.757 - 0.0996s.$$

[6.1]

The experimental data and the model are presented in Figure 6-2.
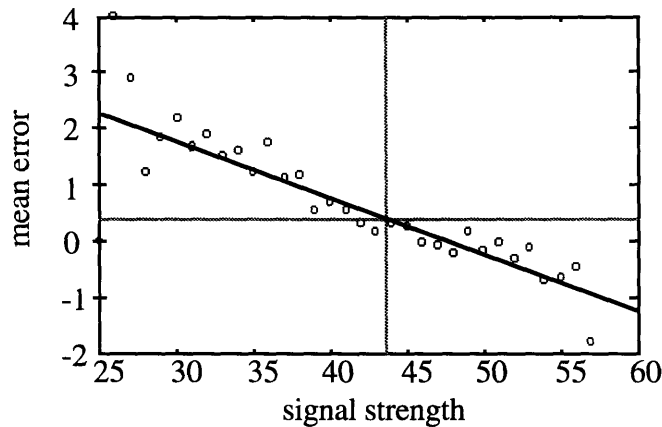
Figure 6-2: Linear regression model for the mean video error as a function of the signal value ($p<0.0001$). The dotted lines indicate the overall mean error (μ_e=0.4044 dB) and the mean signal (μ_s=43.68 dB) from the full data (n=3840). The circles are the mean error computed for each signal value where 5 or more samples were available. The equation of the solid regression line, computed from the full data set, is $\hat{\mu}(s) = 4.757 - 0.0996s$.

47

For a given signal s, the standard deviation of the video error was estimated by linear regression ($p<0.0001$) as:

$$\hat{\sigma}(s) = 4.81 - 0.0526s. \qquad [6.2]$$

This result is presented in Figure 6-3.
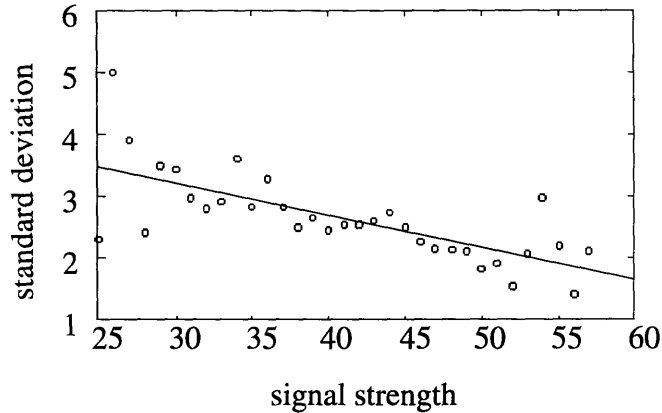
Figure 6-3: Linear regression model for standard deviation of videotape error as a function of signal strength. Both are in decibel units. The circles represent standard deviation estimates calculated at signal strengths where 5 or more samples were present, using the mean found in Equation 6.1. The solid line represents the linear model ($p<0.0001$) calculated from the circle data points ($n=33$) and has the equation $\hat{\sigma}(s) = 4.81 - 0.0526s$.

The expected SNR in decibels, given by

$$SNR_{expected}(s) = 20\log_{10}\left\{s/\hat{\sigma}(s)\right\}, \qquad [6.3]$$

is plotted in Figure 6-4.
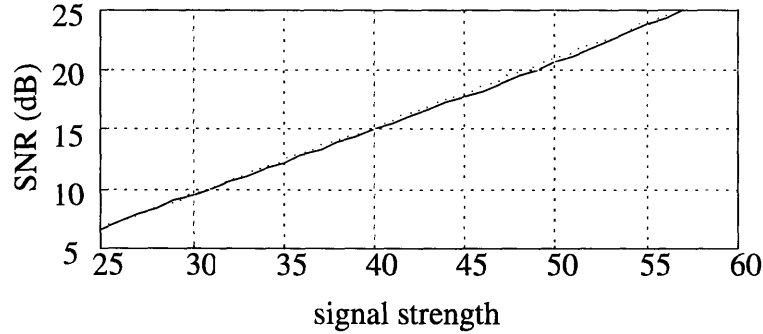
Figure 6-4: Expected Signal-to-Noise ratio as a function of signal strength. The models for signal deviation as a function of signal strength are used to calculate this expected curve, which is shown in the range in which most of the sample points existed. The solid line is the expected SNR, as in Equation 6.3. The dotted line is a straight line passing through the data points at s=25 and 57 to demonstrate that the expected SNR is nearly linear in this region.

The figure shows the values for Equation 6.3 over the range of signal values in which 5 or more data points were present in the sample data set. Although not shown in the figure, as the signal strength approaches zero, the SNR goes to negative infinity by definition since the received signal becomes all noise. In the range presented above, however, the increasing strength and decreasing noise powers balance, leading to an almost linear increase in the expected SNR with increasing signal strength.

Noise autocorrelation

Figure 6-5 shows the average vertical direction autocorrelation function for the corrected noise process, *i.e.* the error corrected for the expected error for the signal strength. This function was found to be very well matched to

$$R_e(\Delta x) \approx \sigma_e^2 \exp\{-|\Delta x|\} \qquad [6.4]$$

for the vertical direction with $\sigma_e^2 = 5.64$. The error is correlated significantly (r>0.1) over only 2 pixels.

49
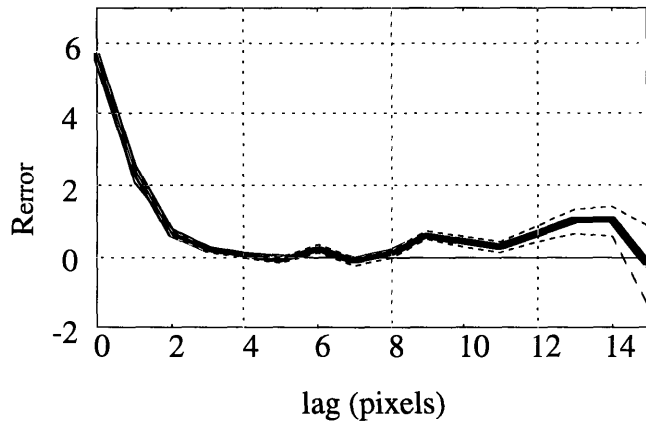
Figure 6-5: Normalized autocovariance function for the corrected videotape noise process. The heavy solid line represents computed values from the data set, the lighter solid line represents the approximating exponential function of equation [6.4] The dashed lines represent the 95% confidence intervals.

Noise crosscorrelation with the signal

The crosscovariance function, presented in Figure 6-6, shows that the corrected error function is not correlated with the signal. The zero-line model fits well within the confidence intervals. As in Figure 6-5, the confidence intervals increase in size with larger lags, a result of the reduced number of samples available from which to calculate the estimate at increased lags.
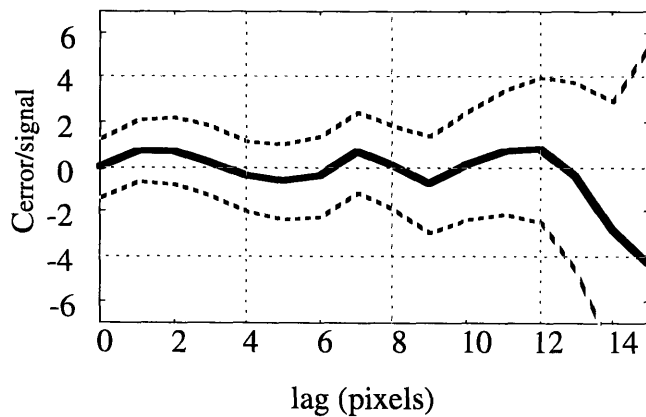
Figure 6-6: The crosscovariance of the corrected error signal with the underlying direct-video digitized signal. The dashed lines represent the 95% confidence intervals for this estimate. Note the increasing size of the interval for larger lags.

6.2 Pathology Specimen Experiments

Resolution

Two pathology sessions were conducted. The zoom resolutions for the first and second sessions were 141 pixels/cm and 107 pixels/cm, respectively.

Off-line TGC Correction

A TGC deviation correction curve was computed for each session in an attempt to correct for operator-dependent variations in the TGC settings. Figure 6-7 shows the TGC deviation corrections computed for pathology sessions 1 and 2.
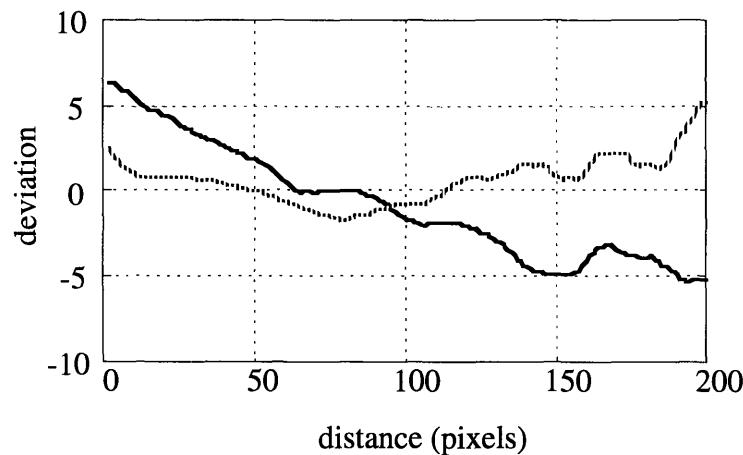
Figure 6-7: Session TGC deviation correction curves. The solid and dotted lines are computed for pathology session 1 and 2, respectively.

Analysis of Variance Results

The autocorrelations of the normalized, corrected images were computed for image intensity *I*. Several summary statistics were computed from the autocorrelations to allow dependent variable analysis of variance on regression models. These summary statistics were the area under the autocovariance curve over the range from 0 to 5 millimeters (abbreviated *auc*), the maximum autocorrelation (*max*), the ratio of the area to the maximum

51

autocovariance (*a/m*), and the full-width at half-maximum (*fwhm*). Models were computed for each of the sessions separately, and also for both sessions together. The results of analysis of variance studies on the computed statistics are presented in Table 6-2.

Table 6-2: Significance Values of Group Parameter from Analysis of Covariance

	Session		
Statistic	**One**	**Two**	**Both**
auc	NS	0.0001	0.005
fwhm	NS	NS	NS
max	NS	0.0171†	NS
a/m	NS	NS	NS

auc=area under curve; *fwhm*=full-width at half-maximum; *max*=maximum autocorrelation value, *a/m*=ratio of area to maximum autocovariance. Set includes normal, HCM, LVH, amyloid, cyclophosphamide and myocarditis groups. NS is noted for $p>0.05$. Unless otherwise noted, in cases where the group is significant, the underlying multiple regression model is significant at the $p<0.05$ level. †Model $p=0.0534$.

Group Statistics

Groups statistics are presented in Tables 6-3, 6-4, and 6-5 for the first session, second session, and combined sessions, respectively. The values listed represent the group average of the specimen sample means for each heart. Summary statistics which were found to show a statistically significant dependence on group are presented in graphical form in Figure 6-8 by group. These statistics are the *auc* and *max* statistics of the second session, and the *auc* statistic of the combined sessions, corrected according to the regression model computed above to the scale of session 2. No combined-sessions area statistic for IDCM or RCM groups is presented because these groups were excluded in the model used to determine the session correction values. Also, session 2 contained no non-amyloid RCM specimens.

Table 6-3: Statistics by Group for First Imaging Session

	Summary Statistic				Number of
	auc	*fwhm*	*max*	*a/m*	Samples
Normal	12.38	0.458	4.42	3.02	1
HCM	12.76	0.511	4.11	3.27	1
Amyloid	12.25 (0.68)	0.544 (0.186)	3.96 (0.25)	3.33 (0.29)	2
IDCM	13.79 (2.09)	0.458 (0.002)	7.57 (4.53)	2.52 (0.85)	2
RCM	10.73	0.458	2.22	4.84	1

Note: Values are presented as mean (standard deviation).

Table 6-4: Statistics by Group for Second Imaging Session

	Summary Statistic				Number of
	auc	*fwhm*	*max*	*a/m*	Samples
Normal	10.62 (0.05)	0.466 (0.013)	2.02 (0.21)	5.36 (0.46)	2
HCM	11.59 (0.15)	0.509 (0.036)	2.06 (0.08)	5.74 (0.25)	2
Amyloid	13.09 (1.14)	0.540 (0.071)	2.66 (0.51)	5.02 (0.46)	3
IDCM	13.03 (2.10)	0.548 (0.051)	2.95 (1.11)	4.85 (0.79)	3
Cyclo-phosphamide	11.06	0.517	2.21	5.08	1
LVH	11.52 (0.55)	0.501 (0.009)	2.11 (0.12)	5.59 (0.13)	2
Myo-carditis	10.56 (0.54)	0.507 (0.027)	1.85 (0.25)	5.85 (1.00)	2

Note: Values are presented as mean (standard deviation).

Table 6-5: Statistics by Group for Both Imaging Sessions Corrected for Session

	Summary Statistic			Number of
	auc	max	a/m	Samples
Normal	11.00 (0.67)	2.19 (0.34)	5.22 (0.40)	3
HCM	11.77 (0.34)	2.12 (0.12)	5.55 (0.36)	3
Amyloid	12.51 (1.18)	2.43 (0.50)	5.11 (0.38)	5
Cyclo-phosphamide	11.06	2.21	5.08	1
LVH	11.52 (0.55)	2.11 (0.12)	5.59 (0.13)	2
Myo-carditis	10.56 (0.54)	1.85 (0.25)	5.85 (1.00)	2

Note: Values are presented as mean (standard deviation).
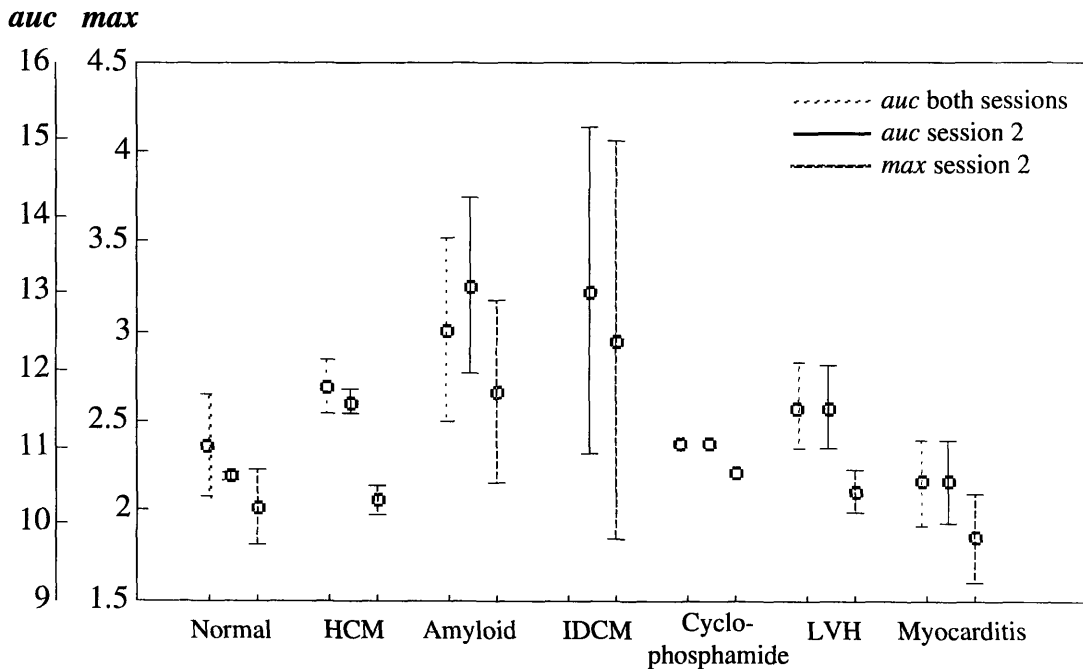
Figure 6-8: Group statistics for summary statistics found to be significantly dependent on group. Circles = mean; error bars = ± one standard deviation. Data (left-to-right): auc for both sessions corrected for session (dotted), auc for session two (solid), and max for session two (dashed). Scalebars are for area values (left) and maximum correlations (right).

6.3 TEE Blood Cavity Experiments

Table 6-6 summarizes the results of fitting normalized image histogram results to the theoretical diffuse model probability distribution for all blood data sets using both the mean fit and error minimization methods. For each subject, the data were collected from the same 10x10 pixel region in the blood cavity data set over all available frames. Slightly better results are observed for minimization of error technique, but error is consistently around 5% (*TSE* as a percentage of *TE*) by either method. The *TSE* and *TE* were defined in Equations 5.3 and 5.4, respectively. Defining TSE as noise energy, and TE as signal energy, this is equivalent to a signal-to-noise ratio of approximately 13 decibels.

Table 6-6: Blood Data Histogram Fitting Results

subject#	TSE% (mean)	(minerr)
1	3.46	3.02
2	4.94	3.77
3	5.60	5.58
4	4.95	4.84
mean	4.74	4.30
standard dev	0.91	1.13

Results for four TEE subjects. The values are total squared-error (*TSE*) as a percentage of the total distribution energy. Different subjects were excluded for showing an observable variation of average intensity in the blood cavity with cardiac cycle, thus widening the observed histogram.

Additionally, the observed histograms were used as input for a chi-square goodness-of-fit test. The results indicated that the observed and theoretical data are statistically different with confidence $p>0.999$ in all cases, even though there is an obvious visual agreement between the observed data and the model. These results are in agreement

with those of Waag *et al.* [1991] who found similar chi-square results in a comparison between the expected Rayleigh distribution and the log-compressed data which were decompressed using calibrated lookup tables.

7. Discussion and Conclusions

7.1 Effects of Videotape Noise on Data Analysis

Ideally, ultrasound scanners would have a digital output for storing image data magnetically or optically. Currently, this is not a feature on commonly available clinical scanners. Although direct-line digitization from the ultrasound scanner to the frame grabber would be the next best arrangement for the collection of the experimental data, clinical conditions make this an extremely difficult setup. In the experiments conducted in this research, space limitations in the operating rooms and examining rooms where the data were collected prevented the transport of the digitizing computer to the data collection site. Until clinical ultrasound scanners are regularly equipped with suitable digital storage devices, videotape is the most feasible way to collect the data.

Video recording is a feature available on almost every commercial scanner. However, the ability to accurately retrieve data from video tape is a controversial subject in the field of ultrasonic tissue characterization. Hence, it was necessary to explore and quantify the signal degradation introduced by this additional link in the experimental setup to determine its effect on the data of interest. In a controlled environment, it was possible to set up the digitizing equipment to directly digitize the data from the scanner, and to record

the exact same data to videotape, and subsequently digitize the playback images for comparison. To eliminate the frame-by-frame playback effects of real-time videotape recording, which are addressed later, each frame from a half-second loop was individually displayed by the scanner and recorded for several seconds, so that a constant picture could be captured with the videotape running at normal playback speed during image digitization. The loop capture function is a standard feature of the machine used in these experiments.

By comparing identical regions of interest in both directly digitized and videotaped images, some conclusions about the nature of signal degradation could be made. For the data analyzed, the mean upward shift introduced by the tape record/playback step was μ=0.4044 digitization intervals (decibels), where a total of 64 intervals (6 bits) were used to match the digitizing board to the ultrasound scanner. Furthermore, this raw error signal was found to have a standard deviation of σ=2.48 digitization intervals (decibels). Although visual inspection of the data presented in Figure 6-1 suggests a simple Gaussian model might be sufficient, some observations about the error signal permit a more accurate description of the noise process.

First, a negative covariance was found between the reference signal and raw error signal. This finding suggests a dependence of the error on signal strength, with higher signal values having a generally lower average error. Early data supported a linear model for error mean as a function of signal strength, so this simplifying assumption was made. The linear regression model of Equation 6.1, presented in Figure 6-2, is highly significant by analysis of variance and agrees with the earlier observations. A similar analysis was performed to estimate the standard deviation of the error as a function of signal strength. Again, a simplifying linear model seemed appropriate in light of early results.

Using the model for the noise variance of Equation 6.2, it is possible to calculate the expected signal to noise ratios as functions of the signal strength. The expected SNR, shown in Figure 6-4, is almost linear in the range presented, which included all signal strengths represented by at least 5 data samples out of a total of 3840. (A uniform

58

distribution would give 60 samples per data value.) The balance between increasing signal strength and decreasing noise powers lead to this almost linear increase. Thus, one would expect the best data, *i.e.* that with the highest SNR, if the equipment is adjusted to the highest possible values without introducing significant clipping errors, assuming that no additional error is introduced in the ultrasound imaging equipment at such settings. In fact, this was the method used to collect data in subsequent experiments.

Noise autocorrelation.

The next step was to determine second order properties of the noise process, *i.e.* to determine whether or not the noise is correlated and whether it is uncorrelated from the signal process. In order to obtain an significant autocorrelation estimate, a stationary process is required. Clearly, the mean of the raw error signal was not stationary. Thus, before computation, the noise was transformed into a zero-mean process by subtracting the expected mean as computed by Equation 6.1 at each point. Although correction for the non-stationary variance may have ultimately provided a better model of the noise, a constant variance was used to reduce model complexity.

The autocorrelation and crosscorrelation curves presented in Figures 6-5 and 6-6, respectively, indicate that the corrected error signal is only slightly correlated, dropping to a correlation coefficient of less than 0.1 in about 2 pixels, and that it is essentially uncorrelated with the signal function. This second result is important because it justifies modeling the noise as a simple additive process, *i.e.* neglecting interaction effects between the signal and the corrected error signal. Since the error noise was found to be slightly correlated, a better estimate of confidence intervals for error statistics might have been made by correcting the number of samples by scaling by the effective correlation cell length, which is the integral of the normalized autocovariance function. Integrating, the effective correlation cell length is approximately 2 pixels, and the effects of this correction would not change any of the conclusions made. Additionally, horizontal correlations were not

examined, and may further increase the correlation cell size, thus further reducing the effective number of independent error samples analyzed.

In summary, the final model presented for the noise is that of correlated Gaussian noise. This model is appropriate after received signals have been corrected for the expected video noise.

Effects of videotape noise on intensity autocorrelation estimates

It is shown in Appendix C.1 that after correction of the signal for the expected video error, the computed autocorrelation estimates for the intensity are corrupted by the video error in a multiplicative way. Specifically, reproducing Equation C.4,

$$R_{12} = \langle I_1 I_2 \rangle E_{12},$$

[7.1]

where E is the multiplicative error scaling, a function of lag, defined in Equation C.5. It is also shown in Appendix C.1 that for properly collected and normalized data, the noise should equally affect all estimates as an upscaling of approximately 39% at zero lag, dropping off to negligible effects over a few pixels as the noise decorrelates. Since this is a relatively limited effect, and one which should equally affect all of the data, the autocorrelation estimates from different images are still directly comparable. Attempts at noise reduction in the compressed signal, while relatively simple for slightly correlated additive Gaussian-like noise, are not desirable because of their modifying effects on the true signal autocorrelation. Many such noise-reduction methods require some knowledge of the shape of autocorrelations of the signal, which is precisely that which this study attempts to determine, and differences in which it attempts to characterize. For these reasons, no noise reduction was attempted other than mean correction, *i.e.* an adjustment of the received signal strength to correct for the expected error associated with that received signal value.

7.2 Off-line TGC Adjustment and Power Normalization

Having provided evidence that the received data collected through the experimental setup are sufficiently uncorrupted by the intermediate storage channel, one must turn to issues related to the operator-dependent variables of the ultrasound scanner. During experimental collections, without the benefit of immediate histogram and gray-level analysis of the recorded images, a few parameters were necessarily adjusted subjectively by the operator to give the "best" picture, namely signal power and TGC settings. Additionally, anatomical variations within living subjects make signal strength and resolution standardization even more challenging. The goal of operator TGC adjustments was to achieve, as best as possible, a uniformity of average signal strength throughout the heart wall imaged.

Variations in signal power, resulting from either the differences in emitted power settings or in attenuation by differing amounts of intervening tissue, are normalized by scaling all uncompressed signals to unit mean. The consequences of operator-introduced variations in TGC settings, however, can be more insidious. An essential assumption of this analysis is that the selected regions of interest represent homogeneous material, *i.e.* a region in which autocorrelation represents has a meaningful physical interpretation. Subtle long-range trends in data introduced by excessive or insufficient TGC may not be readily discernible by the operator during visual examination of the images and adjustment of the ultrasound scanner settings. These hidden trends may introduce unexplainable variations in autocorrelation estimates if they are not considered. The introduction of dropouts and similar undesirable effects by improper TGC adjustment distorts this condition and introduces a more abstruse interpretation of the autocorrelation. For example, a gradual, long-range decrease in received signal strength resulting from insufficient TGC will lead to a "tipping" of the autocorrelation leading to higher values at small lags and lower values at large lags. Thus, before analysis, the data must be examined and corrected for variations in

TGC such that the resulting data are as statistically stationary as possible, *i.e.* closest to the assumption of a homogenous media.

To accomplish the task of vertical TGC normalization, the average deviation of the received signal from the mean signal value has been computed at each depth, *i.e.* vertical position. This deviation function of position was further lowpass filtered with an 11-point moving average filter to leave only the gradual trends that are associated with improper TGC settings. The first and last 5 points of the average were retained unchanged, and the middle kernel was replaced by the moving average output. These computations were performed on the compressed data since attenuation in soft tissues, which TGC attempts to counteract, and the TGC amplification are generally modeled as exponential process, which, upon compression, should be linear. Similarly, errors in TGC settings can be expected to occur in roughly linear sections and are best retained by lowpass filtering.

Since the settings were not changed during the course of each experimental session, and the samples were all imaged at the same distance from the transducer, one would expect the deviations to be similar for all images collected during a given session. Thus, a session average deviation function was computed and subtracted from all signals from that session, completing the TGC normalization.

7.3 Pathologic Grouping Dependence of Summary Statistics

Statistical Results

For the data considered, the area under the curve statistic, computed across the first 5 millimeters of the autocovariance curve, is highly significant in the multiple regression model by analysis of covariance for data from the second session alone, and for data from both sessions after controlling for the session. This suggests that the model coefficient for at least one of the groups is non-zero, *i.e.* the group in at least one of the groups included has a significant effect on expected measure of the area statistic. This evidence supports the

hypothesis that qualities of the autocorrelation change in formalin-fixed tissues in different diseased states. Further experimentation with freshly excised tissues is necessary to be certain that these results are not due solely to different fixation properties of these tissues.

It follows that if the autocorrelation can be described by the generalized model presented in Chapter 4, then some parameter of the model must change in at least one of the pathologic conditions studied. Also, the maximum value statistic taken from the zero-lag value of the autocovariance curve, is also significant, but only for data collected from the second session. But in this case, only a trend towards significance ($p<0.10$) can be noted for the underlying multiple regression model, decreasing confidence in the meaningfulness of the significance of the group in the model. However, there is still a possibility that the maximum value may change in some pathologic conditions.

No significant models were computable for the other statistics: the ratio of the area to the maximum value, and the full-width at half-maximum.

Physical Interpretation of the Computed Measures

The zero-lag values of the computed autocovariance curves are measures of the normalized variability of the data, *i.e.* the variance normalized to the square of the mean, which is also known as the inverse of the signal-to-noise ratio (SNR), or signal contrast. Several parameters of the proposed tissue autocorrelation model could influence these values. Differential effects of changes in the overall diffuse and specular components of the tissue, incorporated into the model as I_d and I_s, respectively, can be analyzed easily by differentiating the model expression with respect to the parameters of interest.

The ratio of the area under the autocovariance curve to its maximum value or zero-lag value, the units of which are distance, is related to a quantity known as the speckle cell size, which is used as a measure of the average size of a speckle "spot" in an image. The speckle cell size S_c is defined by Wagner [1983] as the integral of the unit-normalized autocovariance over all positive and negative lags. Although only the range from 0 to 5

63

millimeters was summed in the experiments reported, it was observed that the computed autocovariances tended to zero in the first 5 millimeters in the data collected. Thus, at the high resolution used to sample the data, the computed ratio should be approximately one-half of the theoretical speckle-cell size.

The area under the curve, then, can be considered as a weighted form of the average speckle cell size. The weighting is maximum value, which has been described above as a measure of normalized variability. The speckle cell size is weighted by the signal contrast, or inverse SNR. It is not surprising that at least one of the two quantities involved also tends towards significance, as indicated above in the statistical analysis of the maximum value. The data suggest that the multiplicative combination of the two values may enhance their overall significance.

The full-width at half-maximum (FWHM) is a rough measure of how quickly the autocovariance drops towards zero. In cases where the autocovariance fits a simple model, the FWHM may be sufficient to completely characterize the curve. However, in more complicated models, its value in describing the autocovariance is greatly reduced. Therefore, it is not disturbing that the regression model for the FWHM including the pathologic group as an independent variable was not statistically significant by analysis of covariance.

7.4 Real-Time Data Collection Videotape Limitations

In order to sequentially digitize and store images from tapes recorded real-time from subjects, the images must be frozen on the screen using the VCR pause function and advanced frame-by-frame with the VCR search function. When playing back videotapes in frame-by-frame freeze-mode on the equipment used in this research, the video tape advances in 1/60th second fields, or half a frame corresponding to either the odd or even lines of the image. The VCR duplicates the interlaced information to fill in the missing lines, resulting in a doubling of the data and a loss of half of the vertical resolution. In

contrast, during the previous experiments where the tape was running at normal playback, both fields were captured simultaneously.

From a signal-processing point of view, this change can be modeled by decimation of the data by a factor of two in the vertical y direction, followed by a two-fold vertical upsampling and convolution with a filter with impulse response $h(r) = \delta(r) + \delta(r - 1)$. From a statistical point of view, this effect will alter second-order statistics. Theoretically, only even lag points in the vertical autocorrelations will represent true data, with odd points interpolated between the adjacent points. This loss of resolution and accuracy was considered when the data were analyzed. From a frequency domain point of view, the original spectrum is compressed to half of its bandwidth, duplicated at the highest frequency, and then multiplied by the frequency response of the aforementioned filter, *i.e.* a two-point periodic sinc function. These facts were also considered when the data were analyzed.

Note that there is no such loss of information in the lateral direction.

7.5 TEE Histogram Statistics

An average error energy of approximately 5% has been determined for the TEE data collected from the blood cavity when compared to the expected histogram. It is argued that since all other parameters are held equal, similar error energies would be expected within the tissue regions if the exact expected histogram shapes were known. More generally, a 5% energy error is representative of the data collection system.

Thus, given a system energy error of about 5%, data values collected with this experimental setup are sufficiently close to the actual compressed values of the radio-frequency amplitude log information that further analysis of these data are justified. A 5% error level corresponds to a signal-to-noise ratio of 13 dB. The low level of this distortion makes it less likely that any results observed are purely the results of equipment variations introduced through processing.

65

Unfortunately, the operating room facilities did not permit direct-line collection of blood cavity data for comparison. These results would be useful in determining at which point the error is introduced. Specifically, such experiments would be useful in determining how much error is present at the scanner output already, and how much is introduced in the transformation to-and-from the analog domain of videotape. Finally, direct results of histogram information determined from the underlying radio-frequency data, corrected for attenuation, would allow the estimation of the error introduced during scan conversion to Cartesian format. This last set of data would also suggest the limitation of the ultrasound machine itself as a data collection method, including the differences in attenuation down each line-of-sight.

Overall, however, this low error rate indicates that off-line videotape analysis of recorded ultrasound examinations does not introduce a great deal of error into the system. As long as all of the resolution matching and freeze-mode considerations are kept in mind, video-based analysis should provide sufficient information with low enough distortion to justify meaningful analysis of the resulting signals.

7.6 Summary and Conclusions

A number of theories modeling the generation of texture in ultrasonic images of tissues were presented. The final model presented a tissue arrangement consisting of both a diffuse randomly arranged component and a statistically defined microstructure. This model predicts that the autocorrelation function computed from image intensities should change to reflect changes in the model parameters. It was proposed that histologic differences in tissues resulting from different pathologic processes lead to changes in these parameters, and hence to a change in the properties of the autocorrelation function. To test this hypothesis, an experimental design was constructed using standard ultrasonic imaging equipment to collect images of pathology laboratory heart tissue specimens. Images were recorded on videotape, and subsequently digitized and analyzed on a computer.

Experiments were conducted to study the effects of the noise introduced by the videotape link on the data. It was concluded that the noise approximates additive Gaussian noise correlated significantly over only two pixels. Theoretical derivations were undertaken to assess the distortion introduced by such noise upon decompression of the image from decibels to intensity. It was found that the effects of the video noise are essentially limited to an upscaling of the main peak value of the autocorrelation, *i.e.* the mean square, by approximately 39%, after the normalizations used in the study. Since this effect was constant, limited, and equally present for all images analyzed, it was judged that the use of videotape was consistent with valid data collection.

Normalizations of the collected images were designed to attempt to correct for two of the user dependencies in the equipment setup: TGC settings and transmission power. Normalized images were computed from laboratory specimens in two separate sessions. Seven different pathologic groups and normal heart specimens were included. Four summary statistics were introduced to simplify statistical analysis of the autocorrelation functions. Upon analysis of variance of linear regression models for these summary statistics, only the area under the autocovariance curve between 0 and 5 millimeters showed a statistically significant ($p<0.005$) dependence on the pathologic grouping over both sessions, although both area and the maximum autocorrelation value were significant ($p=0.0001$ and $p=0.0171$, respectively) for second session samples only. The area under the curve represents the contrast weighted speckle cell size, *i.e.* a variability weighted measure of the size of the speckle "spots" in the axial direction. It was concluded that this summary statistic, and hence the autocorrelation function, may be useful as tools for characterizing tissues using ultrasound.

Lastly, the feasibility of real-time data collection and analysis from living subjects with this experimental design was considered. The implications of continuous videotaping and pause-mode playback for data digitization were considered, particularly the field-by-field advance without interlacing found with the VCR used, and judged to be unlikely to

significantly affect data collection. Images collected from the blood cavities of live subjects using a transesophageal transducer were analyzed, and the resulting distributions compared with theoretical distributions for blood. The distortion was measured by the total squared error as a percentage of the theoretical distribution energy and found to be approximately 5%. It was concluded that real-time collection of data from living subjects with this experimental system is feasible.

In conclusion, this research has indicated that the autocorrelation function computed from digitized images may provide a means of successfully assisting in the characterization of tissues ultrasonically, without the need for biopsies or other invasive procedures or the use of ionizing radiation. Furthermore, although direct digital output from ultrasonic scanners would provide the ideal source of data, the use of videotape to conveniently store image data for later analysis can provide data of sufficient quality for meaningful analysis, even when collected as real-time images from living subjects, and opens to researchers an enormous collection of previously collected clinical images for further study.

Appendix A - Derivations of First-Order Speckle Statistics

A.1 The Diffuse Model: Randomly Arranged Scatterers

If the number of scatterers in a resolution cell is large and they are randomly distributed, the resulting statistics are described as the "fully developed" speckle case. The derivation of the first- and second-order statistics in the similar laser optics case have been carefully studied [Goodman, 1975]. A similar application in narrowband noise in the field of statistical communications [Middleton, 1987] has also yielded analogous results.

When an ultrasound pressure wave interacts with a scatterer much smaller than its wavelength, a weak wave is reradiated omnidirectionally, resulting in a spherical wavefront leaving the scatterer. Neglecting insignificant secondary reflections, *i.e.* applying the Born approximation, each scatterer results in one wave returning towards the transducer. At the range of the transducer, the individual wavelets may be treated as planar. Thus the wavelets from all the scatterers add at the transducer face. The wavelet from a single scatterer s_k can be described by the phasor

$$s_k = \frac{1}{\sqrt{N}}|a_k|\exp\{j\phi_k\}$$

[A.1]

where a_k is the amplitude and ϕ_k is the phase angle associated with the wavelet, and N is the total number of scatterers in the resolution cell. The wavelets will add at the transducer face, giving a resultant phasor A.

If the position of each scatterer is independent and randomly distributed, then the phases of each wavelet will be independent and uniformly distributed over the primary interval $[0,2\pi]$. If the number of wavelets adding at the transducer face is large, the statistics of the complex phasor representing their sum can be treated as the well-studied

random walk problem in the complex plane, and Gaussian statistics can be derived through application of central limit theorems.

The following relations hold for the received phasor A:

$$A_R = \text{Re}\{A\} = \frac{1}{\sqrt{N}} \sum_{k=1}^{N} |a_k| \cos \phi_k$$

$$A_I = \text{Im}\{A\} = \frac{1}{\sqrt{N}} \sum_{k=1}^{N} |a_k| \sin \phi_k \qquad\qquad \text{[A.2a-b]}$$

Since the phase components are independent of the magnitude components, their contributions can be separated in the following expressions for the expectations of the phasor components:

$$\langle A_R \rangle = \frac{1}{\sqrt{N}} \sum_{k=1}^{N} \langle |a_k| \rangle \langle \cos \phi_k \rangle = 0$$

$$\langle A_I \rangle = \frac{1}{\sqrt{N}} \sum_{k=1}^{N} \langle |a_k| \rangle \langle \sin \phi_k \rangle = 0 \qquad\qquad \text{[A.3a-b]}$$

where the solutions $\langle \cos \phi_k \rangle = \langle \sin \phi_k \rangle = 0$ for a phase variable uniformly distributed over the primary interval have been used. Similarly, the variances of these zero-mean random variables can be written:

$$\langle A_R^2 \rangle = \langle A_I^2 \rangle = \frac{1}{N} \sum_{k=1}^{N} \frac{\langle |a_k|^2 \rangle}{2} \qquad\qquad \text{[A.4]}$$

where $\langle \cos^2 \phi_k \rangle = \langle \sin^2 \phi_k \rangle = \frac{1}{2}$ has been used to simplify these equations. Additionally, since $\langle \cos \phi_k \sin \phi_k \rangle = 0$, the two variables must be uncorrelated. In the case of large N, the central limit theorem states that both distributions are approximately Gaussian.

Thus, the real and imaginary parts of the resultant phasor are uncorrelated, identically distributed, Gaussian variables. The joint distribution for the phasor components is simply the product of two independent Gaussian density functions with zero mean and variance defined as σ^2. This distribution is known as a circular Gaussian probability density function (PDF), and can be written as:

$$p_{A_R \cdot A_I}(A_R, A_I) = \frac{1}{2\pi\sigma^2} \exp\left\{-\frac{A_R^2 + A_I^2}{2\sigma^2}\right\} \text{ for } A_R, A_I \geq 0. \qquad \text{[A.5]}$$

First-Order Statistics of Envelope Amplitude and Phase

By applying a statistical transformation, the PDF for the amplitude envelope E and phase angle θ of the phasor can be determined. The following relations hold between the two sets of random variables:

$$A_R = E \cos \theta; \; A_I = E \sin \theta \qquad \text{[A.6]}$$

By transformation methods, the resulting PDF can be solved from:

$$p_{E,\theta}(E,\theta) = p_{A_R,A_I}(E\cos\theta, E\sin\theta) \begin{vmatrix} \delta A_R/\delta E & \delta A_R/\delta\theta \\ \delta A_I/\delta E & \delta A_I/\delta\theta \end{vmatrix} \qquad \text{[A.7]}$$

where the vertical bars indicate the determinant of the enclosed matrix.

Since the ultrasound processor is phase-insensitive, *i.e.* only the envelope of the signal is important, integrating over phase returns the marginal PDF for the envelope amplitude. The B-scanner detects only the envelope of the echo of the transmitted sinusoidal signals, which is ideally the instantaneous amplitude of the phasor. Solving for the envelope PDF:

$$p_E(E) = \frac{E}{\psi} \exp\left\{\frac{-E^2}{2\psi}\right\}, \qquad \text{for } E \geq 0. \qquad \text{[A.8]}$$

where the parameter ψ is a measure of the mean-square scattering strength of the scatterers in the medium:

$$\psi = \sigma^2 = \frac{1}{2N}\sum_{k=1}^{N}\left\langle |a_k|^2 \right\rangle \qquad \text{[A.9]}$$

The distribution in Equation A.8 is known as a Rayleigh PDF. Since the envelope amplitude returning from a resolution cell is proportional to the luminance assigned to the B-mode image for that cell under linear processing, the ultrasonic image of a scattering

71

region meeting the requirements described earlier will exhibit "fully developed" speckle. It is a simple extension to solve for intensity $I = E^2$, which is described by the negative exponential PDF:

$$p_I(I) = \frac{1}{2\psi} \exp\left\{\frac{-I}{2\psi}\right\} \text{ for } I \geq 0.$$ [A.10]

Moments of the Rayleigh PDF

In order to describe the variance of amplitude and intensity, some moments of the amplitude are required. The ν order moment of E is defined as:

$$\langle E^\nu \rangle = \int_0^\infty E^\nu p_E(E) dE.$$ [A.11]

Solving for $\nu=1,2,4$:

$$\langle E \rangle = \sqrt{\frac{\pi\psi}{2}}$$
$$\langle E^2 \rangle = 2\psi = \langle I \rangle$$
$$\langle E^4 \rangle = 8\psi^2 = \langle I^2 \rangle$$ [A.12-14]

Finally, recalling that $I = E^2$, the variances of the envelope E and intensity I can be solved from these moments.

$$\sigma_E^2 = \frac{(4-\pi)\psi}{2}$$
$$\sigma_I^2 = 4\psi^2$$ [A.15-16]

The signal to noise ratio (*SNR*) at a point can be defined as the ratio between the mean and the standard deviation of the signal. Solving:

$$SNR_E = \frac{\pi}{4-\pi} \approx 1.91$$
$$SNR_I = 1$$ [A.17-18]

The inverse of the SNR is known as the speckle contrast. Note that the SNR for both amplitude E and intensity I are both constant, independent of scattering power ψ.

72

First-Order Statistics after Logarithmic Compression

The statistics for the random variable $B = C\log_{10} E$ will be determined. This corresponds to the case in most ultrasound images where logarithmic compression has been used to allow strong and weak echoes to be viewed on the same scale, compressing the dynamic range of the returning signal to better fir within that of the video screen.

Proceeding from the negative exponential PDF for intensity

$$p_I(I) = \frac{1}{2\psi} \exp\left\{\frac{-I}{2\psi}\right\} \quad \text{for } I \geq 0,$$ [A.19]

statistical transformation yields

$$p_B(B) = p_I(I)\frac{\delta I}{\delta B} \qquad \text{for} \qquad I = 10\frac{2B}{C}.$$ [A.20]

Solving, the following PDF is obtained:

$$p_B(B) = \frac{\ln 10}{C\psi} 10^{\frac{2B}{C}} \exp\left\{\frac{-10^{\frac{2B}{C}}}{2\psi}\right\} \quad \text{for } -\infty < B < +\infty.$$ [A.21]

Rewriting:

$$p_B(B) = \frac{\ln 10}{C\psi} \exp\left\{\frac{2B\ln 10}{C} - \frac{\exp[2B\ln 10/C]}{2\psi}\right\} \text{ for } -\infty < B < +\infty.$$ [A.22]

Of course, a video monitor can only display non-negative values of B, so values of B below zero will be *clipped* to zero.

Moments of the logarithmically compressed distribution

The moments of the distribution found above can be expressed as

$$\langle B^v \rangle = \int_{-\infty}^{+\infty} B^v p_B(B) dB.$$ [A.23]

For the first moment in the case of logarithmic compression to decibels, *i.e.* $C=20$, Equations A.22 and A.23 yield:

$$\langle B \rangle = \frac{a}{\psi} \int_{-\infty}^{+\infty} B \exp\left[2aB - \frac{\exp\{2aB\}}{2\psi} \right] dB, \text{ where } a = \frac{\ln 10}{20}.$$ [A.24]

Making the substitution $v = \exp\{2aB\}$:

$$\langle B \rangle = \frac{1}{4a\psi} \int_0^{+\infty} \ln\{v\} \exp\{-v/2\psi\} dv.$$ [A.25]

Making another substitution, $u = v/2\psi$:

$$\langle B \rangle = \frac{1}{2a} \int_0^{\infty} \ln\{2\psi u\} \exp\{-u\} du$$

$$= \frac{1}{2a} \int_0^{\infty} (\ln \psi + \ln 2 + \ln u) \exp\{-u\} du.$$ [A.26]

Splitting into separate integrals and solving:

$$\langle B \rangle = \frac{1}{2a} \left(\ln \psi + \ln 2 + \int_0^{\infty} \ln u \exp\{-u\} du \right)$$

$$= \frac{1}{2a} (\ln \psi + \ln 2 - \gamma)$$

$$\approx 0.5035 + 10 \log_{10} \psi$$ [A.27]

where $\gamma \approx 0.5772$ is Euler's constant. (Below, the integral and γ will be related through the generalized factorial function.) Note that the expected value is directly linear with the scattering strength expressed in decibels. Similarly, solving for the second moment gives:

$$\langle B^2 \rangle = \frac{1}{4a^2} \int_0^{\infty} \ln^2\{2\psi u\} \exp\{-u\} du$$

$$= \frac{1}{4a^2} \int_0^{\infty} (\ln\{2\psi\} + \ln u)^2 \exp\{-u\} du.$$ [A.28]

Splitting Equation A.28 into multiple integrals and solving as in Equation A.27 yields:

$$\langle B^2 \rangle = \frac{1}{4a^2} \left[\ln\{2\psi\}(\ln\{2\psi\} - 2\gamma) + \int_0^{\infty} \ln^2 u \exp\{-u\} du \right].$$ [A.29]

The remaining integral can be solved by noting that it is equivalent to the second derivative of the generalized factorial function $\Gamma(z) = \int_0^\infty t^{z-1} \exp\{-t\} dt$ evaluated at $z=1$, which is solved to:

$$\Gamma''(1) = \int_0^\infty \ln^2 t \exp\{-t\} dt = \gamma^2 + \frac{\pi^2}{6} \qquad [\text{A.30}]$$

Thus, Equation A.29 reduces to:

$$\left\langle B^2 \right\rangle = \frac{1}{4a^2} \left[\ln^2\{2\psi\} - 2\gamma \ln\{2\psi\} + \gamma^2 + \frac{\pi^2}{6} \right]. \qquad [\text{A.31}]$$

Finally, the variance of B can be found using Equations A.31 and A.27:

$$\begin{aligned} \sigma_B^2 &= \frac{1}{4a^2} \left[\ln^2\{2\psi\} - 2\gamma \ln\{2\psi\} + \gamma^2 + \frac{\pi^2}{6} - \left(\ln\{2\psi\} - \gamma \right)^2 \right] \\ &= \frac{1}{4a^2} \left[\frac{\pi^2}{6} \right] \\ &\approx 31 \end{aligned} \qquad [\text{A.32}]$$

Note that the variance is a constant, independent of the scattering power ψ, indicating that the curves of this family of probability distributions have constant shape.

A.2 Intermediate Model: Constant Structural Component

In this section, the statistics of speckle in the presence of a constant background structural signal will be determined. This case is analogous to the random walk described above with the addition of a constant phasor of amplitude S to the wavelets summing at the transducer face. Without loss of generality, the angle of the constant phasor will be set to zero. Thus the resulting PDF for the components of the resultant phasor will still be circular Gaussian with equal variances, but the mean will be shifted to as required by the constant phasor. The new PDF can be written as

$$p_{A_R,A_I}(A_R,A_I) = \frac{1}{2\pi\sigma^2}\exp\left\{-\frac{(A_R+S)^2+A_I^2}{2\sigma^2}\right\} \quad \text{for } A_R,A_I \geq 0. \qquad [A.33]$$

Applying the same transformation described above, and solving for the marginal PDF for intensity, the following PDF is obtained

$$p_I(I) = \frac{1}{2\psi}\exp\left\{\frac{-(I+S^2)}{2\psi}\right\}I_0\left\{\frac{S\sqrt{I}}{\psi}\right\} \quad \text{for } I \geq 0. \qquad [A.34]$$

where $I_0(...)$ is a modified Bessel function of the first kind and zero order:

$$I_0(k) = \frac{1}{2\pi}\int_{-\pi}^{+\pi}\exp\{k\cos\theta\}d\theta. \qquad [A.35]$$

The PDF for I has been named in the literature as the modified Rician density, since I is the square of the Rician random variable, the amplitude E.

Moments of the Modified Rician PDF

As described by Middleton [1987], the moments of I can be found through the relation:

$$\langle I^v \rangle = (2\psi)^v\, v!\,_1F_1\left(-v;1;\frac{S^2}{2\psi}\right) \qquad [A.36]$$

where $_1F_1(a;b;c)$ is the confluent hypergeometric function. The first two moments of I are:

$$\langle I \rangle = 2\psi + S^2$$
$$\langle I^2 \rangle = 8\psi^2 + 8\psi S^2 + S^4. \qquad [A.37\text{-}38]$$

From these moments, the Rician variance can be calculated:

$$\sigma_I^2 = \langle I^2 \rangle - \langle I \rangle^2$$
$$= 4\psi^2 + 4\psi S^2. \qquad [A.39]$$

Note that this model no longer has a constant signal to noise ratio, and always exceeds unity for a nonzero structural component amplitude S. These results can also be derived

76

from the autocorrelation result found in Appendix B, in a manner similar to that shown in the next section.

A.3 Generalized Rician Model: Statistically Defined Structural Component

First-order statistics in the Generalized Rician model are easiest solved from the autocorrelation function derived and explained in Appendix B, rewritten below:

$$\langle I_1 I_2 \rangle = I_d^2 \left[1 + |\rho|^2 \right] + 2I_d \langle I_s \rangle + \langle I_{s1} \otimes I_{s2} \rangle + 2I_d \langle R_1 \otimes R_2 + I_1 \otimes I_2 \rangle \rho. \qquad [A.40]$$

The first order moments can be found with the following substitutions:

$$\langle I_1 I_2 \rangle = \left\{ \begin{matrix} \langle I^2 \rangle \\ \langle I \rangle^2 \end{matrix} \right\} \quad \text{when} \quad \rho = \left\{ \begin{matrix} 0 \\ 1 \end{matrix} \right\}. \qquad [A.41]$$

Solving, one obtains:

$$\langle I^2 \rangle = 2I_d^2 + \langle I_s^2 \rangle + 4I_d \langle I_s \rangle$$
$$\langle I \rangle = I_d + \langle I_s \rangle \qquad [A.42]$$

which can be solved for the variance of the intensity I:

$$\sigma_I^2 = I_d^2 + \langle I_s^2 \rangle + 2I_d \langle I_s \rangle - \langle I_s \rangle^2$$
$$= \sigma_{I_d}^2 + \sigma_{I_s}^2 + 2I_d \langle I_s \rangle$$
$$= 4\psi^2 + \sigma_{I_s}^2 + 4\psi \langle I_s \rangle \qquad [A.43]$$

where $\sigma_{I_s}^2$ is the variance of the intensity of the specular component. Note for the case of zero specular variance, *i.e.* a constant specular component, Equation A.43 reduces as expected to Equation A.39.

Appendix B - Derivations of Second-Order Speckle Statistics

B.1 Second-Order Statistics in the Absence of Background Signal

The properties of texture are described by the second-order statistics of the random variable. The correlation properties for the amplitude envelope E and intensity I in the pure diffuse, "fully developed" speckle case are described below. The statistic of interest is the autocorrelation function.

The autocovariance $K_x(r_1, r_2)$ of a random variable x defined over a region is related to its autocorrelation function $R_x(r_1, r_2)$ such that:

$$K_x(r_1, r_2) + \langle x(r_1) \rangle \langle \overline{x}(r_2) \rangle = R_x(r_1, r_2) = \langle x(r_1) \cdot \overline{x}(r_2) \rangle \qquad [\text{B.1}]$$

where $\langle ... \rangle$ denotes the expected value, r_1, r_2 are two image positions, and the overbar denotes complex conjugation.

To derive the autocorrelation function for the echo amplitude E and intensity I, some statistical properties of linear systems will be used. First, the received complex phasor A, described in detail in Appendix A.1, will be modeled as the convolution of the scatterer point position process R and the symmetric system point spread function (PSF) g, such that:

$$A(r) = R(r) * g(r), \qquad [\text{B.2}]$$

where the asterisk denotes the aperiodic convolution operator, R describes the spatial distribution of the complex scattering amplitude of the scatterers, and g describes the ultrasonic beam geometry. As before, A is a zero mean process whose first-order statistics are described by a circular Gaussian probability distribution. Solving for the autocorrelation of A, treating g as a deterministic function and R as a stationary process, gives:

$$R_A(\Delta r) = g(-\Delta r) * \overline{g}(\Delta r) * R_R(\Delta r) \qquad [B.3]$$

where $R_R(\Delta r)$ is the autocorrelation of R. The last term of Equation B.3 can be rewritten as:

$$R_R(\Delta r) = \left\langle R(r) \cdot \overline{R}(r + \Delta r) \right\rangle$$
$$\approx \left\langle |R(r)|^2 \right\rangle \cdot \mu_R(\Delta r) \qquad [B.4]$$

In these equations, $\mu_R(\Delta r)$ is the normalized microscopic autocorrelation. Setting the average scattering strength to the constant R_0^2 in the region of interest, the autocorrelation of A can be simplified to:

$$R_A(\Delta r) = g(\Delta r) * \overline{g}(\Delta r) * R_R(\Delta r)$$
$$= g(\Delta r) * \overline{g}(\Delta r) * R_0^2 \cdot \mu_R(\Delta r) \qquad [B.5]$$
$$= R_0^2 \cdot g(-\Delta r) * \overline{g}(\Delta r) * \mu_R(\Delta r)$$

If the microstructure is assumed to be random and uncorrelated, then $\mu_R(\Delta r) = \delta(\Delta r)$, the Dirac delta fuction, and the autocorrelation of A is only a function of the point-spread function and the average scattering strength. Since the point spread function can always be modeled as a real function [Wagner,1983], the autocorrelation will also be real. So, the speckle texture only carries information about the system PSF. For a symmetrical PSF, Equation B.5 simplifies to:

$$R_A(\Delta r) = R_0^2 \cdot g(\Delta r) * g(\Delta r) \qquad [B.6]$$

For the amplitude envelope $E = |A|$, the autocorrelation can be determined from the general results found in statistical communication theory [Middleton, 1987]:

$$\left\langle E^m(x) E^n(x + \Delta x) \right\rangle = (2\psi)^{(m+n)/2} \Gamma(m/2 + 1)$$
$$\times \Gamma(n/2 + 1) {}_2F_1\left(-m/2, -n/2; 1; |k(\Delta x)|^2\right) \qquad [B.7]$$

where ${}_2F_1$ is the Gaussian hypergeometric function and Γ is generalized factorial and

$$k(\Delta x) = \frac{R_A(\Delta x)}{R_A(0)} = \frac{\left\langle A_1 \overline{A}_2 \right\rangle}{\left\langle I \right\rangle} \qquad [B.8]$$

is the normalized autocovariance function for A also called the complex coherence factor ρ or μ. The subscripts 1 amd 2 in the last term of Equation B.8 have been introduced for notational simplicity, and correspond to x and $x+\Delta x$. The autocorrelation of the amplitude envelope E is given for the case $m = n = 1$, which reduces to:

$$R_E(\Delta x) = (\pi\psi/2)_2 F_1\left(-1/2, -1/2; 1; |k(\Delta x)|^2\right)$$
$$= \psi\left[2E_1\left(|k(\Delta x)|\right) - \left(1 - |k(\Delta x)|^2\right)E_2\left(|k(\Delta x)|\right)\right] \qquad \text{[B.9]}$$

where $E_1(...), E_2(...)$ are elliptical integrals of the first and second kind, respectively. For intensity I, the solution simplifies to:

$$R_I(\Delta r) = \langle I \rangle^2\left(1 + |k(\Delta r)|^2\right) = \langle I \rangle^2 + \left|\langle A_1 \overline{A}_2 \rangle\right|^2. \qquad \text{[B.10]}$$

Clearly, the results for the intensity I are much easier to manipulate, and therefore, the autocorrelation of the intensity is the function studied in the experiments of this work. The same result has been obtained by Goodman [1975] in the field of laser optics. Equation B.10 can also be found more simply using the Gaussian moments theorem [Bendat, 1971], which states that for four zero-mean Gaussian random variables:

$$\langle x_1 x_2 x_3 x_4 \rangle = \langle x_1 x_2 \rangle\langle x_3 x_4 \rangle + \langle x_1 x_3 \rangle\langle x_2 x_4 \rangle + \langle x_1 x_4 \rangle\langle x_2 x_3 \rangle \qquad \text{[B.11]}$$

Applying the moment theorem to the complex Gaussian phasor A :

$$\langle I_1 I_2 \rangle = \langle A_1 \overline{A}_1 A_2 \overline{A}_2 \rangle$$
$$= \langle A_1 \overline{A}_1 \rangle\langle A_2 \overline{A}_2 \rangle + \langle A_1 A_2 \rangle\langle \overline{A}_1 \overline{A}_2 \rangle + \langle A_1 \overline{A}_2 \rangle\langle \overline{A}_1 A_2 \rangle \qquad \text{[B.12]}$$
$$= \langle I_1 \rangle\langle I_2 \rangle + \left|\langle A_1 A_2 \rangle\right|^2 + \left|\langle A_1 \overline{A}_2 \rangle\right|^2$$

Recalling that real and imaginary parts of A have the same variance and are uncorrelated, the second term of Equation B.12 can be elliminated by substituting $A = r + ji$:

$$\langle A_1 A_2 \rangle = \langle r_1 r_2 \rangle - \langle i_1 i_2 \rangle + j\langle r_1 i_2 \rangle + j\langle i_1 r_2 \rangle$$
$$= \sigma^2 - \sigma^2 + j \cdot 0 + j \cdot 0 \qquad \text{[B.13]}$$
$$= 0$$

Thus the system reduces to:

$$\langle I_1 I_2 \rangle = \langle I_1 \rangle \langle I_2 \rangle + \left| \langle A_1 \overline{A_2} \rangle \right|^2 \qquad \text{[B.14]}$$

which is equivalent to Equation B.10. For yet another derivation of equation B.14 using the moments theorem, interested readers are referred to the work of Wagner, *et al.* [1988].

B.2 Intermediate Model: Constant Structural Component

Rewriting intensity in terms of its real and imaginary components r and i, and using a fixed background vector length S and phase zero gives:

$$\begin{aligned}
\langle I_1 I_2 \rangle &= \left\langle \left[(r_1 + S)^2 + i_1^2 \right] \cdot \left[(r_2 + S)^2 + i_2^2 \right] \right\rangle \\
&= \left\langle \left(r_1^2 + i_1^2 \right) \left(r_2^2 + i_2^2 \right) \right\rangle \\
&\quad + \left\langle \left(r_1^2 + i_1^2 + S^2 + 2Sr_1 \right) \left(S^2 + 2Sr_2 \right) + \left(r_2^2 + i_2^2 \right) \left(S^2 + 2Sr_1 \right) \right\rangle
\end{aligned} \qquad \text{[B.15]}$$

The first term corresponds to the solution from the diffuse case of Section B.1. Expanding the second term gives:

$$\begin{aligned}
\langle I_1 I_2 \rangle &= I_d^2 \left[1 + |\rho|^2 \right] + S^2 \left\langle r_1^2 + i_1^2 + r_2^2 + i_2^2 \right\rangle + S^4 + 4 S^2 \left\langle r_1 r_2 \right\rangle \\
&\quad + 2 S^3 \left\langle r_1 + r_2 \right\rangle + 2 S \left\langle r_2 \left(r_1^2 + i_1^2 \right) \right\rangle + 2 S \left\langle r_1 \left(r_2^2 + i_2^2 \right) \right\rangle
\end{aligned} \qquad \text{[B.16]}$$

The subscript d has been introduced in the first term to indicate that it is the expected diffuse component of the signal, as found in the previous section. Recall that the expected value of both r and i is zero at all positions. Thus, by treating S as a Gaussian random variable with zero variance, the moment theorem (Equation B.11) can be applied to terms in Equation B.16 with odd powers of S to demonstrate that they must equal zero. Simplifying the remaining terms, and substituting $I_s = S^2$ to represent the structural component of the signal gives:

$$\begin{aligned}
\langle I_1 I_2 \rangle &= I_d^2 \left[1 + |\rho|^2 \right] + I_s \left\langle I_{d1} + I_{d2} \right\rangle + I_s^2 + 4 I_s \left\langle r_1 r_2 \right\rangle \\
&= I_d^2 \left[1 + |\rho|^2 \right] + 2 I_d I_s + I_s^2 + 2 I_d I_s \rho
\end{aligned} \qquad \text{[B.17]}$$

B.3 Generalized Rician Model: Statistically Defined Structural Component

Using a similar process as that used above, the autocorrelation of intensity I in the case of statistically defined specular contributions can be found:

$$\langle I_1 I_2 \rangle = I_d^2 \left[1 + |\rho|^2 \right] + 2I_d \langle I_s \rangle + \langle I_{s1} I_{s2} \rangle + 2I_d \langle r_1 r_2 + i_1 i_2 \rangle \rho \qquad \text{[B.18]}$$

where r and i now denote the real and imaginary components of the strucutural intensity I_s, respectively. Readers interested in a detailed derivation of Equation B.18 are referred to Wagner *et al.* [1985].

Appendix C- Other Derivations

C.1 Effects of the Video Error on Autocorrelation Estimates

The issue of assessing how much the noise introduced by videotape storage affects the data of interest when computing the autocorrelation of the intensities, as described in Chapter 4, is addressed by considering the decompression of the received data. Since the data collected has been recorded in a full logarithmic compression mode setting of the machine, the signal values represent a decibel equivalent of the actual amplitude as described earlier. To reconvert to intensity I, the following relation must be applied:

$$I = \exp(s \ln 10 / 10) = 10^{s/10} \qquad [\text{C.1}]$$

(Note: Although the digitizing board used in this research actually returns values which are multiples of four, this factor of four is explicitly removed by the data processing programs and for clarity is not included in this discussion) When the videotape noise is added in, one obtains:

$$\tilde{I} = \exp\{(s + e) \ln 10/10\} \qquad [\text{C.2}]$$

The tilda mark over intensity is used to indicate that it is not the true value, but the received signal which is corrupted by the videotape channel noise. Thus, computing the autocorrelation gives:

$$R_{12} = \left\langle \tilde{I}_1 \tilde{I}_2 \right\rangle = \left\langle \exp\{(s_1 + e_1) \ln 10/10\} \exp\{(s_2 + e_2) \ln 10/10\} \right\rangle \qquad [\text{C.3}]$$

Note that the subscripts 1 and 2 have been used in place of the more conventional x and $x+\Delta x$ to simplify notation. At this point we will assume that the error noise e at every position is zero mean and uncorrelated with the signal. In Section 6.1, it was shown that

these assumptions are justified when the expected mean error $\hat{\mu}(s)$ is subtracted from the received signal. Thus, Equation C.3 can be rewritten:

$$\begin{aligned}
R_{12} &= \left\langle \exp\{(s_1 + s_2)\ln 10/10\} \exp\{(e_1 + e_2)\ln 10/10\}\right\rangle \\
&= \left\langle I_1 I_2 \right\rangle \left\langle \exp\{(e_1 + e_2)\ln 10/10\}\right\rangle \\
&= \left\langle I_1 I_2 \right\rangle E_{12}
\end{aligned} \qquad \text{[C.4]}$$

In order to solve for the error multiplier E, not to be confused with the envelope amplitude used elsewhere, certain simplifying assumptions must be made. Specifically, the noise is assumed to be Gaussian with the autocovariance properties found in Section 6.1. This assumption is reasonable since the noise has an approximately Gaussian distribution and characteristics. In order to simplify notation, the $\ln 10/10$ factor will be incorporated in the variable e and the appropriate scaling of the standard deviations and correlations will be made. This factor will be extracted at the conclusion of the derivation. Thus,

$$\begin{aligned}
E_{12} &= \left\langle \exp\{e_1 + e_2\}\right\rangle \\
&= \int_{-\infty}^{+\infty}\int_{-\infty}^{+\infty} \exp\{e_1' + e_2'\} p_{e_1,e_2}(e_1',e_2')\,de_1''de_2'' \\
&= \iint \exp(e_1'' + e_2'') N(e_1'',e_2'';0,0;\sigma,\sigma,r_{12})\,de_1''de_2'',
\end{aligned} \qquad \text{[C.5]}$$

where $N(x,y;\mu_x,\mu_y;\sigma_1,\sigma_2,r)$ is the joint normal distribution for x and y and r is the correlation coefficient. At a given lag, r is found from the autocorrelation found for the error function as given by Equation 6.4, normalized by the variance. The distribution N in Equation C.5 is given by Papoulis [1991]:

$$N_{12}(e_1,e_2;\ldots) = \frac{1}{2\pi\sigma_e^2\sqrt{1-r_{12}^2}} \exp\left[\frac{-1}{2(1-r_{12}^2)}\left(\frac{e_1^2 + e_2^2 - 2r_{12}e_1e_2}{\sigma^2}\right)\right]. \qquad \text{[C.6]}$$

Solving Equation C.6 is tedious, but easily accomplished with careful substitutions:

$$E_{12} = \frac{1}{2\pi\sigma_e^2\sqrt{1-r_{12}^2}}\iint\exp\left[\frac{1}{2\sigma_e^2\left(1-r_{12}^2\right)}\right.$$
$$\left.\cdot\left\{-e_1^2 - e_2^2 + 2r_{12}e_1e_2 + 2\sigma_e^2\left(1-r_{12}^2\right)\left(e_1+e_2\right)\right\}\right]de_1de_2$$

$$= \frac{1}{\sqrt{2\pi}\sigma_e}\iint\frac{1}{\sqrt{2\pi\sigma_e^2\left(1-r_{12}^2\right)}}\exp\left[\frac{1}{2\sigma_e^2\left(1-r_{12}^2\right)}\right.$$
$$\left.\cdot\left\{-e_2^2 + 2e_2\left[r_{12}e_1 + \sigma_e^2\left(1-r_{12}^2\right)\right]\right\}\right]de_2$$

$$\cdot\exp\left[\frac{1}{2\sigma_e^2\left(1-r_{12}^2\right)}\left\{-e_1^2 + 2\sigma_e^2\left(1-r_{12}^2\right)e_1\right\}\right]de_1 \qquad [\text{C.7}]$$

Solving the inner integral by completing the square in the exponential:

$$\int...de_2 = \int\frac{1}{\sqrt{2\pi\sigma_e^2\left(1-r_{12}^2\right)}}\exp\left[\frac{1}{2\sigma_e^2\left(1-r_{12}^2\right)}\right.$$
$$\cdot\left\{-\left(e_2 - \left[r_{12}e_1 + \sigma_e^2\left(1-r_{12}^2\right)\right]\right)^2\right.$$
$$\left.\left.+\left[r_{12}e_1 + \sigma_e^2\left(1-r_{12}^2\right)\right]^2\right\}\right]de_2$$

$$= \exp\left[\frac{\left[r_{12}e_1 + \sigma_e^2\left(1-r_{12}^2\right)\right]^2}{2\sigma_e^2\left(1-r_{12}^2\right)}\right]$$
$$\cdot\int N\left\{e_2;\mu = r_{12}e_1 + \sigma_e^2\left(1-r_{12}^2\right),\sigma^2 = \sigma_e^2\left(1-r_{12}^2\right)\right\}de_2$$

$$= \exp\left[\frac{\left[r_{12}e_1 + \sigma_e^2\left(1-r_{12}^2\right)\right]^2}{2\sigma_e^2\left(1-r_{12}^2\right)}\right] \qquad [\text{C.8}]$$

where N is a Gaussian distribution with the given parameters. Substituting the result of Equation C.8 back into Equation C.7:

$$E_{12} = \frac{1}{\sqrt{2\pi}\sigma_e}\int\exp\left[\frac{1}{2\sigma_e^2\left(1-r_{12}^2\right)}\left\{\left[r_{12}e_1 + \sigma_e^2\left(1-r_{12}^2\right)\right]^2\right.\right.$$
$$\left.\left.-e_1^2 + 2\sigma_e^2\left(1-r_{12}^2\right)e_1\right\}\right]de_1$$

$$= \frac{1}{\sqrt{2\pi}\sigma_e}\int\exp\left[\frac{1}{2\sigma_e^2\left(1-r_{12}^2\right)}\left\{-e_1^2\left(1-r_{12}^2\right)\right.\right.$$
$$\left.\left.+2e_1\sigma_e^2\left(1-r_{12}^2\right)\left(1+r\right) + \sigma_e^4\left(1-r_{12}^2\right)^2\right\}\right]de_1 \qquad [\text{C.9}]$$

Cancelling terms in Equation C.9:

85

$$E_{12} = \frac{1}{\sqrt{2\pi}\sigma_e} \int \exp\left[\frac{1}{2\sigma_e^2}\left\{-e_1^2 + 2e_1\sigma_e^2(1+r_{12}) + \sigma_e^4(1-r_{12}^2)\right\}\right] de_1$$

$$= \frac{1}{\sqrt{2\pi}\sigma_e} \int \exp\left[\frac{1}{2\sigma_e^2}\left\{-\left(e_1 - \sigma_e^2\{1+r_{12}\}\right)^2 \right.\right.$$
$$\left.\left. + \left[\sigma_e^2(1+r_{12})\right]^2 + \sigma_e^4(1-r_{12}^2)\right\}\right] de_1$$

$$= \exp\left[\frac{\sigma_e^4}{2\sigma_e^2}\left(1 + 2r_{12} + r_{12}^2 + 1 - r_{12}^2\right)\right]$$
$$\cdot \int N\left(e_1; \mu = \sigma_e^2\{1+r_{12}\}, \sigma^2 = \sigma_e^2\right) de_1 \qquad [C.10]$$

Finally, solving and cancelling terms in Equation C.10 and replacing the subscripts 1 and 2 with the more conventional x and $x+\Delta x$, and extracting the $\ln 10/10$ factor:

$$E(\Delta x) = \exp\left[\frac{\sigma_e^2 \ln^2 10}{100}(1 + r(\Delta x))\right] = \exp\left[\frac{\ln^2 10}{100}(\sigma_e^2 + R_e(\Delta x))\right] \qquad [C.11]$$

Thus, with Equation C.11, the multiplicative scaling E applied to the autocorrelation estimates in Equation C.4 can be estimated for any lag if an estimate of the error autocorrelation is known. To characterize the effects of the error, however, one may look specifically at two points of interest, those of maximum and minimum autocorrelation, i.e. lags zero and infinity. At these points, the multiplicative factors from Equation C.11 can be solved to be $\exp\{2\sigma_e^2 \ln^2 10/100\}$ and $\exp\{\sigma_e^2 \ln^2 10/100\}$, respectively. To assess the effect on the data to be considered, a standard deviation of 2.5, as found in the sample data of Section 6.1, is considered. In this case, the multiplicative factors are 1.94 and 1.39, respectively, resulting in a zero-lag scaling of 1.39 or 39% after division by the received mean, which will also be upscaled by 1.39. Since the actual distribution found in section 6.1 is even narrower than the corresponding Gaussian curve, we might expect an even smaller effect. Since variance appears to rise as signal decreases, the upscaling effect would also increase at lower average signal values.

In summary, the effects of videotape noise on the calculated autocorrelation curves for data collected near the high end of the signal range should be an upscaling of the main peak of approximately 39%, quickly dropping off to no effect over a few pixels as the

noise error decorrelates. It is important to realize that data collected in a consistent manner with respect to the average signal strength will always be consistently and equally affected by a scaling factor and can thus be compared directly.

C.2 The Correlation Cell Size

The correlation cell size S_C is a measure of the average size of the speckle spot in a given direction. It is defined by:

$$S_C = \int_{-\infty}^{\infty} \frac{C_I(\Delta x)}{C_I(0)} d(\Delta x),$$ [C.12]

where C is the autocovariance function of intensity I. For the Rayleigh case, the speckle cell size in the axial direction reduces to:

$$S_C = \int_{-\infty}^{\infty} |\rho(\Delta x)|^2 d(\Delta x).$$ [C.13]

Correlation is actually two dimensional in ultrasound scanning. The lateral or transverse dimension of the structure is due to the shape of the diffraction and focusing pattern, and the axial or range dimension is due to the shape of the pulse in the range direction. Assuming that beam phase at a given range in constant lateral phase, the point spread function can be factored into separate functions for the axial and transverse directions [Wagner et al., 1988]. In Appendix A, it was found that ρ is determined by the point spread function in the axial direction.

Thus, in the case of fully developed speckle with a Gaussian beam pulse envelope, the correlation cell size is proportional to the standard deviation of the pulse length. Stated differently, the axial cell size is exclusively and inversely dependent on the transducer bandwidth [Thijssen,1990].

References

[1] Bamber JC and Dickinson RJ, "Ultrasonic B-scanning: a computer simulation", Physics in Medicine and Biology, 25:463-479, 1980.

[2] Burckhardt CB, "Speckle in Ultrasound B-Mode Scans", IEEE Transactions on Sonics and Ultrasonics, SU-25:1-6, 1978.

[3] Chandrasekaran K, Aylward PE, Fleagle SR, Burns TL, Seward JB, Tajik AJ, Collins SM and Skorton DJ, "Feasibility of Identifying Amyloid and Hypertrophic Cardiomyopathy with the Use of Computerized Quantitative Texture Analysis of Clinical Echocardiographic Data", Journal of the American College of Cardiology, 13:832-840, 1989.

[4] Dainty JC, "An Introduction to 'Gaussian' Speckle", SPIE Vol. 243 Applications of Speckle Phenomena, 1980, pp.2-8.

[5] Dickinson RJ, "A Computer Model for Speckle in Ultrasound Images", *Acoustical Imaging*, Vol. 10, Metherell AF, ed., Plenum Press, New York, 1982, pp.115-129.

[6] Dyer RAG, Dyer SA and Bhagat PK, "Myocardial Tissue Characterization Using Pattern Recognition Procedures on Backscattered Ultrasonic Signals", Ultrasonic Imaging, 8:181-195, 1986.

[7] Fellingham LL and Sommer FG, "Ultrasonic Characterization of Tissue Structure in the *In Vivo* Human Liver and Spleen", IEEE Transactions of Sonics and Ultrasonics, SU-31, 1984, 418-428.

[8] Finette S, "A Computer Model of Acoustic Wave Scattering in Soft Tissue", IEEE Transactions on Biomedical Engineering, BME-34:336-344, 1987.

[9] Flax SW, Glober GH and Pelc NJ, "Textural Variations in B-Mode Ultrasonography: A Stochastic Model", Ultrasonic Imaging, 3:235-257, 1981.

[10] Foster DR, Arditi M, Foster FS, Patterson MS and Hunt JW, "Computer Simulations of Speckle in B-scan Images", Ultrasonic Imaging 5:308-330, 1983.

[11] Fraker TD Jr., Nelson AD, Arthur JA and Wilkerson RD, "Altered Acoustic Reflectance on Two-Dimensional Echocardiography as an Early Predictor of Myocardical Infarc Size", American Journal of Cardiology 53:1699-1702, 1984.

[12] Galloway MM, "Texture Analysis Using Gray Level Run Lengths", Computer Graphics and Image Processing, 4:172-179, 1975.

[13] Goodsitt MM, Madsen EL, Zagzebski JA, "A Three Dimenstional Model for Generating the Texture in B-Scan Ultrasound Images", Ultrasonic Imaging, 5:253-279, 1983.

[14] Goodman JW, "Statistical Properties of Laser Speckle Patterns", in *Laser Speckle and Related Phenomena*, Dainty JC, ed., Springer-Verlag, Berlin, 1975, pp.9-75.

[15] Goodman JW, "A Random Walk through the Field of Speckle", SPIE Vol. 556 International Conference on Speckle, 1985, pp.2-5.

[16] Guyton, AC. *Textbook of Medical Physiology*, 8th edition, WB Saunders, Philadelphia, 1991, ch.32-33.

[17] Haendchen RV, Ong K, Fishbein MC, Zwehl W, Meerbaum S and Corday E, "Early Differentiation of Infarcted and Noninfarcted Reprefused Myocardium in Dogs by Quantitative Analysis of Regional Myocardial Echo Amplitudes", Circulation Research 57:718-728, 1985.

[18] Hishida H, Sakabe Y, Kawamura K, Hagiwara K, Murashima Y, Kodama K, Sugiura Y, Koyama Y, Tamagaki H, Fukui M and Mizuno Y, "Evaluation of Cardiac Tissue from Two-Dimensional Echocardiogram: Analysis of Gray Level and Its Distribution", Japanese Circulation Journal, 54:316-321, 1990.

[19] Insana MF, Wagner RF, Garra BS, Brown DG and Shawker TH, "Analysis of Ultrasound Image Texture via Generalized Rician Statistics", SPIE Vol. 556 International Conference on Speckle, 1985, pp.153-159.

[20] Insana MF and Hall TJ, "Characterising the Microstructure of Random Media Using Ultrasound", Physics in Medicine and Biology 35:1373-1386, 1990.

[21] Jacobs EMGP and Thijssen JM, "A Simulation Study of Echographic Imaging of Diffuse and Structurally Scatttering Media", Ultrasonic Imaging 13:316-333, 1991.

[22] Jensen JA, "A Model for the Propagation and Scattering of Ultrasound in Tissue", Journal of the Acoustical Society of America, 89:182-190, 1991.

[23] Kauczor H-U, Fein M, Zuna I, Delorme S, Suhm N, Knopp MV and van Kaick G, "Texture Analysis of B-Scan Images: Transferability between Different Ultrasound Scanners", *Acoustical Imaging*, Vol. 19, Ermert H and Harjes H-P, eds., Plenum Press, New York, 1992, pp.393-397.

[24] Landini L, Santarelli F, Paterni M, Verrazzani L, Christ A and Hein HJ, "Echo Signal Processing in Medical Ultrasound", *Acoustical Imaging*, Vol. 19, Ermert H and Harjes H-P, eds. Plenum Press, New York, 1992, pp.387-391.

[25] Lapin GD, Sullivan BJ and Paul MH, "Tissue Characterization by Spectral Analysis of Ultrasound Images", *Acoustical Imaging*, Vol. 16, Kessler LW, ed., Plenum Press, New York, 1988, pp.329-338.

[26] Lee B and Park SB, "Modeling and Computer Simulation of Ultrasound Imaging Systems and Human Tissues", Ultrasonic Imaging 10:229-247, 1988.

[27] Leeman S and Jones JP, "Tissue Information from Ultrasound Scattering", *Acoustical Imaging*, Vol.13, Kaveh M, ed., Plenum Press, New York, 1984, pp.233-245.

[28] Lizzi FL, Ostromogilsky M, Feleppa EJ, Rorke MC and Yaremko MM, "Relationship of Ultrasonic Spectral Parameters to Features of Tissue Microstructure", IEEE Transactions on Ultrasonics, Ferroelectrics, and Frequency Control, UFFC-33:319-329, 1986.

[29] Lizzi FL, "New Developments in Ultrasonic Tissue Characterization", *Acoustical Imaging*, Vol. 19, Ermert H and Harjes H-P, eds., Plenum Press, New York, 1992, pp.353-362.

[30] Logan-Sinclair R, Wong CM and Gibson DG, "Clinical Application of Amplitude Processing of Echocardiographic Images", British Heart Journal, 45:621, 1981.

[31] Lythall DA, Gibson DG, Kushwaha SS, Norell MS, Mitchell AG and Ilsley CJD, "Changes in Myocardial Echo Amplitude During Reversible Ischaemia in Humans", British Heart Journal, 67:368-376, 1992.

[32] Madaras EI, Barzilai B, Perez JE, Sobel BE and Miller JG, "Changes in Myocardial Backscatter throughout the Cardiac Cycle", Ultrasonic Imaging, 5:229-239, 1983.

[33] Martin RP, Rakowski H, French J and Popp RL, "Idiopathic Hypertrophic Subaortic Stenosis Viewed by Wide-angle, Phased-array Echocardiography", Circulation, 59:1206-1217, 1979.

[34] Masuyama T, St. Goar FG, Tye TL, Oppenheim G, Schnittger I and Popp RL, "Ultrasonic Tissue Characterization of Human Hypertrophied Hearts in vivo with Cardiac Cycle-Dependent Variation in Integrated Backscatter", Circulation, 80:925-934, 1989.

[35] Masuyama T, Valantine HA, Gibbons R, Schnittger I and Popp RL, "Serial Measurements of Integrated Ultrasonic Backscatter in Human Cardiac Allografts for the Recognition of Acute Rejection", Circulation, 81:829-839, 1990.

[36] McPherson DD, Aylward PE, Knosp BM, Bean JA, Kerber RE, Collins SM, and Skorton DJ, "Ultrasound Characterization of Acute Myocardial Ischemia by Quantitative Texture Analysis", Ultrasonic Imaging, 8:227-240, 1986.

[37] Middleton D, *An Introduction to Statistical Communication Theory*, Peninsula Publishing, Los Altos, California, 1987, ch.9 and appendices.

[38] Milunski MR, Mohr GA, Perez JE, Vered Z, Wear K, Gessler CJ, Sobel BE, Miller JG and Wickline SA, "Ultrasonic Tissue Characterization with Integrated Backscatter", Circulation 80:491-503, 1989.

[39] Mimbs JW, Bauwens D, Cohen Rd, O'Donnell M, Miller Jg and Sobel Be, "Effects of Myocardial Isshemia on Quantitative Ultrasonic Backscatter and Identification of Responsible Determinants", Circulation Research, 49:89-96, 1981.

[40] Nicholas D, Nassiri DK, Garbutt P and Hill CR, "Tissue Characterization from Ultrasound B-Scan Data", Ultrasound in Medicine and Biology, 12:135-143, 1986.

[41] Ohya A, Kashioka J and Nakajima M, "Ultrasonic Speckle Region and Extra-Speckle Condition", *Acoustical Imaging*, Vol. 19, Ermert H and Harjes H-P, eds., Plenum Press, New York, 1992, pp.109-114.

[42] Oosterveld BJ, Thijssen JM and Verhoef WA, "Texture of B-Mode Echograms: 3-D Simulations and Experiments of the Effects of Diffraction and Scatterer Density", Ultrasonic Imaging, 7:142-160, 1985.

[43] Oosterveld BJ, Thijssen JM, Hartman PC, Romijn RL and Rosenbusch GJE, "Ultrasound Attenuation and Texture Analysis of Diffuse Liver Disease: Methods and Preliminary Results", Physics in Medicine and Biology, 36:1039-1064, 1991.

[44] Parisi AF, Nieminen M, O'Boyle JE, Moynihan PF, Khuri SF, Kloner RA, Follan ED and Schoen FJ, "Enhanced Detection of the Evolution of Tissue Changes after Acute Myocardial Infarction using Color-Encoded Two-Dimensional Echocardiography", Circulation, 66:764, 1982.

[45] Pingitore A, Kozakova M, Picano E, Paterni M, Landini L, Distante A, "Acute Myocardial Gray Level Intensity Changes Detected by Transesophageal Echocardiography During Intraoperative Ischemia", American Journal of Cardiology, 72:465-469, 1993.

[46] Papoulis A. Probability, Random Variables, and Stochastic Processes, 3d ed. McGraw-Hill, New York, 1991. ch.6.

[47] Rasmussen S, Corya BC, Feigenbaum H and Knoebel SB, "Detection of Myocardial Scar Tissue by M-mode Echocardiography", Circulation, 57:230-237, 1978.

[48] Rhyne TL and Sagar KB, "IBR5: An Optimal Measurement of Integrated Backscatter and Cyclic Variation of Integrated Backscatter", Ultrasonic Imaging 12:189-204, 1990.

[49] Rosner B, *Fundamentals of Biostatistics*, PWS-Kent, Boston, Massachussetts, 1990, ch. 10.

[50] Sagar KB, Pelc LR, Rhyne TL, Howard J and Warltier DC, "Estimation of Myocardial Infarct Size with Ultrasonic Tissue Characterization", Circulation 83:1419-1428, 1991.

[51] Siqueira-Filho AG, Cunha CLP, Tajik AJ, Seward JB, Schattenburg TT, Giuliani ER, "M-Mode and Two-Dimensional Echocardiographic Features in Cardiac Amyloidosis", Circulation, 63:188-196, 1981.

[52] Shung KK, Sigelmann RA and Reid JM. "Scattering of Ultrasound by Blood", IEEE Transactions on Biomedical Engineering, 23:460-467, 1976.

[53] Skorton DJ, Collins SM, Nichols J, Pandian NG, Bean JA and Kerber RE, "Quantitative Texture Analysis in Two-Dimensional Echocardiography: Application to the Diagnosis of Experimental Myocardial Contusion", Circulation, 68:217, 1983.

[54] Skorton DJ, Collins SM, Garcia E, Geiser EA, Hillard W, Koppes W, Linker D and Schwartz G, "Digital Signal and Image Processing in Echocardiography", American Heart Journal, 110:1266-1283, 1985.

[55] Skorton DJ and Collins SM, "Characterization of Myocardial Structure with Ultrasound", in *Tissue Characterization with Ultrasound*, Vol. 2, Greenleaf JF, ed., CRC Press, Boca Raton, Florida, 1986, pp.123-146.

[56] Skorton DJ, Miller JG, Wickline S, Barzilai B, Collins SM and Perez JE, "Ultrasonic Characterization of Cardiovascular Tissue", in *Cardiac Imaging*, Marcus ML, *et al.*, eds., W.B. Saunders Co., Philadelphia, Pennsylvania, 1991, pp.538-556.

[57] Sleefe GE, *Acoustic Backscatter from Random Media: Signal Modelling, Parameter Estimation, and Application to Ultrasonic Tissue Characterization*, Ph.D. Thesis, MIT, 1987.

[58] Smith SW, Sandrik JM, Wagner RF and van Ramm OT, "Measurements and Analysis of Speckle in Ultrasound B-Scans", *Acoustical Imaging*, Vol. 10, Metherell AF, ed., Plenum Press, New York, 1982, pp.195-211.

[59] Smith SW and Wagner RF, "Ultrasound Speckle Size and Lesion Signal to Noise Ratio: Verification of Theory", Ultrasonic Imaging 6:174-180, 1984.

[60] Smith SW, Trahey GE, Hubbard SM and Wagner RF, "Properties of Acoustical Speckle in the Presence of Phase Aberration Part II: Correlation Lengths", Ultrasonic Imaging 10:29-51, 1988.

[61] Solomon SD, Kytomaa H, Celi A, Maas LC, Hopkins J, Chou L, Caguioa E and Lee RT, "Two Dimensional Autocorrelation for Tissue Characterization", submitted for publication, 1994.

[62] Steinmetz E, Brennecke R, Schmidtmann I and Erbel R, "Echocardiographic Image Analysis Based on the Evaluation of First Order Speckle Statistics", *Acoustical Imaging*, Volume 19, Ermert H and Harjes H-P, eds., Plenum Press, New York, 1992, pp.381-385.

[63] Stempfle H-U, Angermann CE, Kraml P, Schutz A, Kemkes BM and Theisen K, "Serial Changes During Acute Cardiac Allograft Rejection: Quantitatitve Ultrasound Tissue Analysis versus Myocardial Histologic Findings", Journal of the American College of Cardiology, 22:310-317, 1993.

[64] Tanigawa G, Jarcho JA, Kass S, Solomon SD, Vosberg H-P, Seidman JG, Seidman CE, "A Molecular Basis for Familial Hypertrophic Cardiomyopathy: An α/β Cardiac Myosin Heavy Chain Hybrid Gene", Cell, 62:991-998, 1990.

[65] Thijssen JM, Oosterveld BJ and Wagner RF, "Gray Level Transforms and Lesion Detectability in Echographic Images", Ultrasonic Imaging 10:171-195, 1988.

[66] Thijssen JM and Oosterveld BJ, "Texture in Tissue Echograms: Speckle or Information?", Journal of Ultrasound in Medicine, 9:215-229, 1990.

[67] Thijssen JM, Oosterveld BJ, Hartman PC and Rosenbusch GJE, "Correlations between Acoustic and Texture Parameters from RF and B-Mode Liver Echograms", Ultrasound in Medicine and Biology 19:13-20, 1993.

[68] Tuthill TA, Sperry RH and Parker KJ, "Deviations from Rayleigh Statistics in Ultrasonic Speckle", Ultrasonic Imaging 10:81-89, 1988.

[69] Vered Z, Mohr GA, Barzilai B, Gessler CJ, Wickline Sa, Wear KA, Shoup TA, Weiss AN, Sobel BE, Miller JG and Perez JE, "Ultrasonic Integrated Backscatter Tissue Characterization of Remote Myocardial Infarction in Human Subjects", Journal of the American College of Cardiology, 13:84-91, 1989.

[70] Waag RC, "A Review of Tissue Characterization from Ultrasonic Scattering", IEEE Transactions on Biomedical Engineering, BME-31:884-893, 1984.

[71] Waag RC, Demczar BA and Case TJ, "Nonlinear Reciever Compression Effects on the Amplitude Distribution of Backscattered Ultrasonic Signals", IEEE Transactions on Biomedical Engineering 38:628-633, 1991.

[72] Wagner RF, Smith SW, Snadrik JM and Lopez H, "Statistics of Speckle in Ultrasound B-Scans", IEEE Transactions on Sonics and Ultrasonics, SU-30:156-163, 1983.

[73] Wagner RF, Insana MF and Brown DG, "Unified Approach to the Detection and Classification of Speckle Texture in Diagnostic Ultrasound", SPIE Vol. 556 International Conference on Speckle, 1985, pp.146-152.

[74] Wagner RF, Insana MF and Brown DG, "Statistical Properties of Radio-Frequency and Envelope-Detected Signals with Applications to Medical Ultrasound", Journal of the Optical Society of America A, 4: 910-922, 1987.

[75] Wagner RF, Insana MF and Smith SW, "Fundamental Correlation Lengths of Coherent Speckle in Medical Ultrasonic Images", IEEE Transactions on Ultrasonics, Ferroelectrics, and Frequency Control, UFFC-35:34-44, 1988.

[75] Wickline SA, Thomas LJ III Miller JG, Sobel BE and Perez JE, "The Dependence of Myocardial Ultrasonic Backscatter on Contractile Performance", Circulation, 72:183-192, 1985.

[76] Wickline SA, Verdonk ED, Sobel BE and Miller JG, "Identification of Human Myocardial Infarction *In Vitro* Based on the Frequency Dependence of Ultrasonic Backscatter", Journal of the Acoustical Society of America, 91:3018-3025, 1992.